Article

Cell Reports

IL-33-PU.1 Transcriptome Reprogramming Drives Functional State Transition and Clearance Activity of Microglia in Alzheimer's Disease

Graphical Abstract

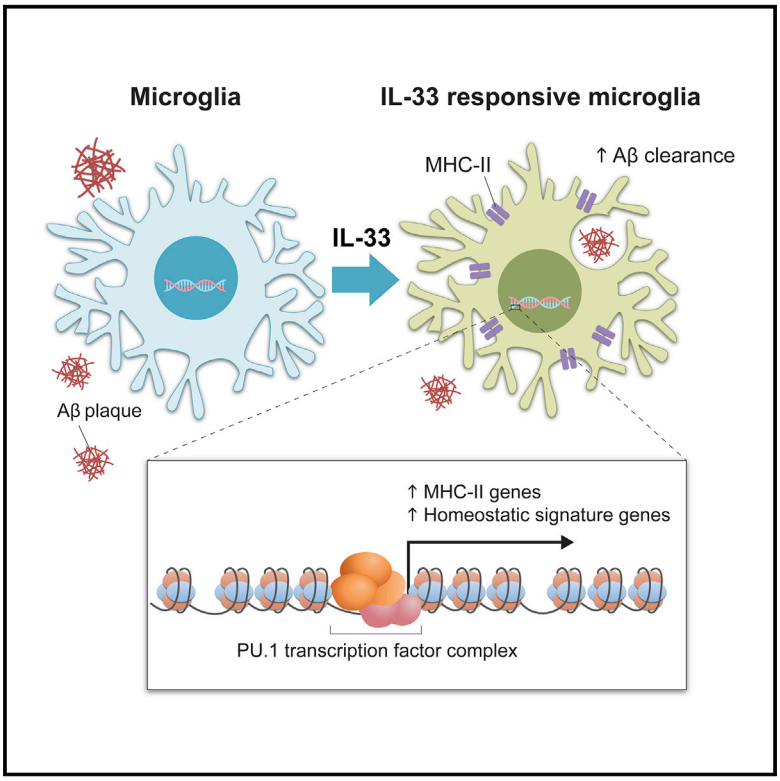

Highlights

- IL-33 induces a MHC-II-expressing microglial subpopulation in AD
- IL-33-responsive microglia exhibit increased Aβ clearance activity
- Chromatin state controls the transcriptome signature of IL-33-responsive microglia
- PU.1 activity is required for the microglial Aβ clearance stimulated by IL-33

Authors

Shun-Fat Lau, Congping Chen, Wing-Yu Fu, Jianan Y. Qu, Tom H. Cheung, Amy K.Y. Fu, Nancy Y. Ip

Correspondence

boip@ust.hk

In Brief

Lau et al. show that interleukin-33 (IL-33) enhances microglial amyloid-beta clearance by inducing a subpopulation of MHC-II+ phagocytic microglia, which is, in turn, controlled by PU.1-dependent transcriptome reprogramming. Thus, the authors reveal an IL-33-PU.1 axis involved in transcriptional regulation that promotes beneficial microglial functions in Alzheimer's disease.

Lau et al., 2020, Cell Reports *31*, 107530
April 21, 2020
https://doi.org/10.1016/j.celrep.2020.107530

CellPress

Cell Reports
Article

IL-33-PU.1 Transcriptome Reprogramming Drives Functional State Transition and Clearance Activity of Microglia in Alzheimer's Disease

Shun-Fat Lau,[1,2,3] Congping Chen,[2,4,5] Wing-Yu Fu,[1,2,3] Jianan Y. Qu,[2,4,5] Tom H. Cheung,[1,2] Amy K.Y. Fu,[1,2,3,6] and Nancy Y. Ip[1,2,3,6,7,*]

[1]Division of Life Science, The Hong Kong University of Science and Technology, Clear Water Bay, Hong Kong, China
[2]State Key Laboratory of Molecular Neuroscience, The Hong Kong University of Science and Technology, Clear Water Bay, Hong Kong, China
[3]Molecular Neuroscience Center, The Hong Kong University of Science and Technology, Clear Water Bay, Hong Kong, China
[4]Biophotonics Research Laboratory, Department of Electronic and Computer Engineering, The Hong Kong University of Science and Technology, Clear Water Bay, Hong Kong, China
[5]Center of Systems Biology and Human Health, School of Science and Institute for Advanced Study, The Hong Kong University of Science and Technology, Clear Water Bay, Hong Kong, China
[6]Guangdong Provincial Key Laboratory of Brain Science, Disease and Drug Development, HKUST Shenzhen Research Institute, Shenzhen-Hong Kong Institute of Brain Science, Shenzhen, Guangdong 518057, China
[7]Lead Contact
*Correspondence: boip@ust.hk
https://doi.org/10.1016/j.celrep.2020.107530

SUMMARY

Impairment of microglial clearance activity contributes to beta-amyloid (Aβ) pathology in Alzheimer's disease (AD). While the transcriptome profile of microglia directs microglial functions, how the microglial transcriptome can be regulated to alleviate AD pathology is largely unknown. Here, we show that injection of interleukin (IL)-33 in an AD transgenic mouse model ameliorates Aβ pathology by reprogramming microglial epigenetic and transcriptomic profiles to induce a microglial subpopulation with enhanced phagocytic activity. These IL-33-responsive microglia (IL-33RMs) express a distinct transcriptome signature that is highlighted by increased major histocompatibility complex class II genes and restored homeostatic signature genes. IL-33-induced remodeling of chromatin accessibility and PU.1 transcription factor binding at the signature genes of IL-33RM control their transcriptome reprogramming. Specifically, disrupting PU.1-DNA interaction abolishes the microglial state transition and Aβ clearance that is induced by IL-33. Thus, we define a PU.1-dependent transcriptional pathway that drives the IL-33-induced functional state transition of microglia, resulting in enhanced Aβ clearance.

INTRODUCTION

Microglia, the primary innate immune cells in the brain, maintain the immune homeostasis of the central nervous system (CNS) milieu through immunosurveillance, neurotrophic support, and synaptic pruning (Ransohoff and El Khoury, 2016; Schafer and Stevens, 2015). Perturbation of CNS homeostasis due to the accumulation of misfolded proteins, myelin debris, or apoptotic cells triggers microglial activation. The activated microglia adopt a phagocytic phenotype in order to restrain cytotoxicity and limit damage to surrounding cells (Kierdorf and Prinz, 2013; Ransohoff and Perry, 2009; Song and Colonna, 2018). During neurodegeneration, genetic risk factors, systemic inflammation, and the accumulation of aging-related factors in the CNS milieu impair microglial homeostatic functions, which consequently contributes to the pathology of many neurodegenerative diseases, including Alzheimer's disease (AD) (Mosher and Wyss-Coray, 2014; Perry and Teeling, 2013).

AD, the most common form of dementia, is characterized by extracellular protein deposits of misfolded beta-amyloid (Aβ) peptides and neurofibrillary tangles comprising hyperphosphorylated Tau protein. The deposition of Aβ plaques triggers a microglial response, wherein microglia migrate toward Aβ plaques to initiate phagocytosis (Hansen et al., 2018; Meyer-Luehmann et al., 2008). However, as AD progresses, the microglia become dysfunctional, resulting in impaired clearance of misfolded Aβ peptides, inefficient barrier formation around Aβ plaques, and increased secretion of amyloid-seeding factors (Condello et al., 2015; Mosher and Wyss-Coray, 2014; Perry and Holmes, 2014; Wang and Colonna, 2019). In turn, these lead to further accumulation of Aβ plaques, concurrent with synaptic impairment and neuronal death in AD (DiSabato et al., 2016). Intriguingly, enhancing Aβ clearance activity of microglia by modulating cytokine milieus in the CNS—such as replenishing interleukin (IL)-33 or inhibiting IL-10, IL-12/IL-23, or the NLRP3 inflammasome—results in reduced Aβ pathology and improved cognitive performance in AD transgenic mouse models (Vom Berg et al., 2012; Fu et al., 2016; Guillot-Sestier et al., 2015; Heneka et al., 2013). Specifically, in Aβ deposition mouse models, IL-33 injection enhances Aβ phagocytosis by microglia, reduces the level of pro-inflammatory cytokines in the CNS milieu, and improves cognitive performance (Fu et al., 2016).

Recent single-cell RNA-sequencing (scRNA-seq) analysis in AD mouse models revealed that homeostatic microglia gradually acquire the state of disease-associated microglia (DAMs) (also

called neurodegenerative [MGnD] or activated-response microglial [ARM]; hereinafter referred to as "DAMs") (Keren-Shaul et al., 2017; Krasemann et al., 2017; Sala Frigerio et al., 2019). Transcriptome profiling has shown that this microglial subpopulation highly expresses genes associated with pattern recognition, lipid metabolism, and lysosomal pathways, including *Apoe*, *Axl*, *Cst7*, *Lpl*, and *Trem2* (Fourgeaud et al., 2016; Kim et al., 2009; Ulrich et al., 2018; Wang et al., 2015). These pathways are crucial regulators of phagocytic processes, including detection, engulfment, and degradation. While further studies are required to determine how the transcriptome signature of the DAM state drives functional impairment of microglia, particularly at different AD stages, manipulating microglial functions through reprogramming its transcriptome signature is a potential therapeutic strategy against AD. Indeed, both IL-33 injection and NLRP3 inflammasome inhibition, which yield beneficial outcomes in AD mouse models, regulate the transcriptome signature of microglia (Fu et al., 2016; Heneka et al., 2013). However, the molecular pathways that reprogram the dysregulated microglial phenotype in AD, resulting in beneficial outcome, remain unclear.

In the present study, we show that IL-33 injection induces a transcriptionally distinct DAM subpopulation that is characterized by the increased expression of major histocompatibility complex class II (MHC-II) genes and the restored expression of some homeostatic signature genes. This subpopulation of microglia, named IL-33-responsive microglia (IL-33RMs), exhibits higher Aβ phagocytic capacity and lysosomal activity than other DAM subpopulations and, thus, contributes to the enhanced Aβ clearance in IL-33-injected AD transgenic mice. Epigenetic profiling shows that the induction of IL-33RMs is controlled by the remodeling of chromatin accessibility and PU.1 binding at the signature genes of this microglial subpopulation. Together, our findings demonstrate an IL-33-induced epigenetic and transcriptional regulation of microglial state transition that contributes to the alleviation of AD pathology.

RESULTS

IL-33 Enhances the Chemotactic Response of a Microglial Subpopulation toward Aβ Plaques in APP/PS1 Mice

IL-33 injection enhances the co-localization of microglia with Aβ plaques and promotes Aβ clearance (Fu et al., 2016). To investigate how IL-33 regulates the dynamic interaction of microglia with Aβ plaques, we performed time-lapse *in vivo* two-photon imaging of microglia and Aβ deposition in APP/PS1;Cx3cr1^{eYFP} mice (Figures 1A, 1B, and S1A). We first examined the chemotactic responses of microglia to Aβ plaques by measuring the distance they traveled and the change in distance relative to the nearest Aβ plaques. In vehicle-injected (Con) APP/PS1 mice, the microglia remained relatively stationary over 12 h, traveling only 8.0 ± 0.5 μm (Figure 1C), which is less than the average soma diameter of microglia (Kozlowski and Weimer, 2012). In contrast, IL-33 injection increased the average mobility of microglia to 13.9 ± 0.5 μm (Figure 1C). Specifically, IL-33 induced a highly mobile microglial subpopulation (traveling ≥30 μm in 12 h) from 1.8% to 11.0% of the total microglial population (Figure 1D). This highly mobile microglial subpopulation migrated closer to the nearby Aβ plaques after IL-33 injection (Figures 1E, 1F, and S1B). Meanwhile, the ramification of microglia, which indicates microglial projections surveying the surrounding area (Madry et al., 2018), remained relatively unchanged in APP/PS1 mice following IL-33 injection (Figure S1C). These findings demonstrate that IL-33 enhances the Aβ chemotactic responses of a microglial subpopulation, resulting in their recruitment to Aβ plaques.

Upon recruitment to Aβ plaques, microglia react with Aβ through barrier formation or phagocytosis—the latter of which results in Aβ clearance (Heneka et al., 2015). Recent studies also revealed that Aβ-plaque-associated microglia acquire a distinct transcriptome profile characterized by the expression of DAM markers (e.g., *Cst7*) (Keren-Shaul et al., 2017; Sala Frigerio et al., 2019). Consistently, our RNA fluorescence *in situ* hybridization (FISH) analysis showed that IL-33 injection increased the number of DAMs (i.e., *Cst7*$^+$ *Cx3cr1*$^+$ cells) that were associated with Aβ plaques by 17.7% (Figures 1G, 1H, S1D, and S1E).

IL-33 Induces a Microglial Subpopulation that Expresses MHC-II and Homeostatic Signature Genes

The functions of microglia can be elucidated on the basis of their transcriptome signature (Crotti and Ransohoff, 2016; Hickman et al., 2013). Since IL-33 induces a subpopulation of microglia with enhanced chemotactic and phagocytic activity, we examined the regulation of the microglial transcriptome in APP/PS1 mice upon IL-33 injection. Accordingly, we conducted scRNA-seq analysis of the myeloid (i.e., CD11b$^+$) cells in the forebrain in APP/PS1 mice after IL-33 injection. Unsupervised clustering of 15,041 CD11b$^+$ cells using the t-Distributed Stochastic Neighbor Embedding (t-SNE) algorithm identified seven unique cell clusters based on transcriptome signatures: DAMs (*Cst7*$^+$ and *Igf1*$^+$), endothelial cells (*Igfbp7*$^+$ and *Ptprb*$^+$), granulocytes (*Camp*$^+$ and *Ngp*$^+$), homeostatic microglia (*Cilp2*$^+$ and *Lrba*$^+$), oligodendrocytes (*Mobp*$^+$ and *Tubb4a*$^+$), oligodendrocyte precursor cells (*Mki67*$^+$ and *Top2a*$^+$), and perivascular macrophages/monocytes (*Cd209a*$^+$ and *Mrc1*$^+$) (Figures 2A and 2B) (Keren-Shaul et al., 2017; Li et al., 2019).

Next, we analyzed the transcriptome reprogramming of microglia upon IL-33 injection and found that IL-33 increased the expression of genes that are associated with antigen presentation (e.g., *Cd74*, *Ciita*, *H2-Aa*, *H2-Ab1*, *H2-DMa*, *H2-DMb1*, and *H2-Eb1*) and actin filament organization (e.g., *Cap1*) while reducing those associated with lipid metabolism (e.g., *Nrp1*, *Spp1*, and *Lpl*) in microglia in APP/PS1 mice (Figures 2C and S2A). Some of these differentially expressed genes (DEGs)—including *Cap1*, *Fcrls*, *Mlph*, *Sft2d1*, *Lpl*, *Nrp1*, and *Spp1*—were dysregulated in APP/PS1 mice when compared to the wild-type littermates (Figure S2B; Tables S1 and S2) (Butovsky et al., 2014; Hickman et al., 2013; Kang et al., 2018; Ofengeim et al., 2017). IL-33-induced transcriptional changes in the microglia of APP/PS1 mice were negatively correlated with the changes in microglial gene expression induced by Aβ deposition, suggesting that IL-33 was able to restore some of these transcriptomic changes (Figure 2D; Table S2). Of note, the proportion of DAMs remained unchanged in APP/PS1 mice after IL-33 injection (Figures S2C and S2D), showing that the restoration was not due to a decrease in the DAM proportion.

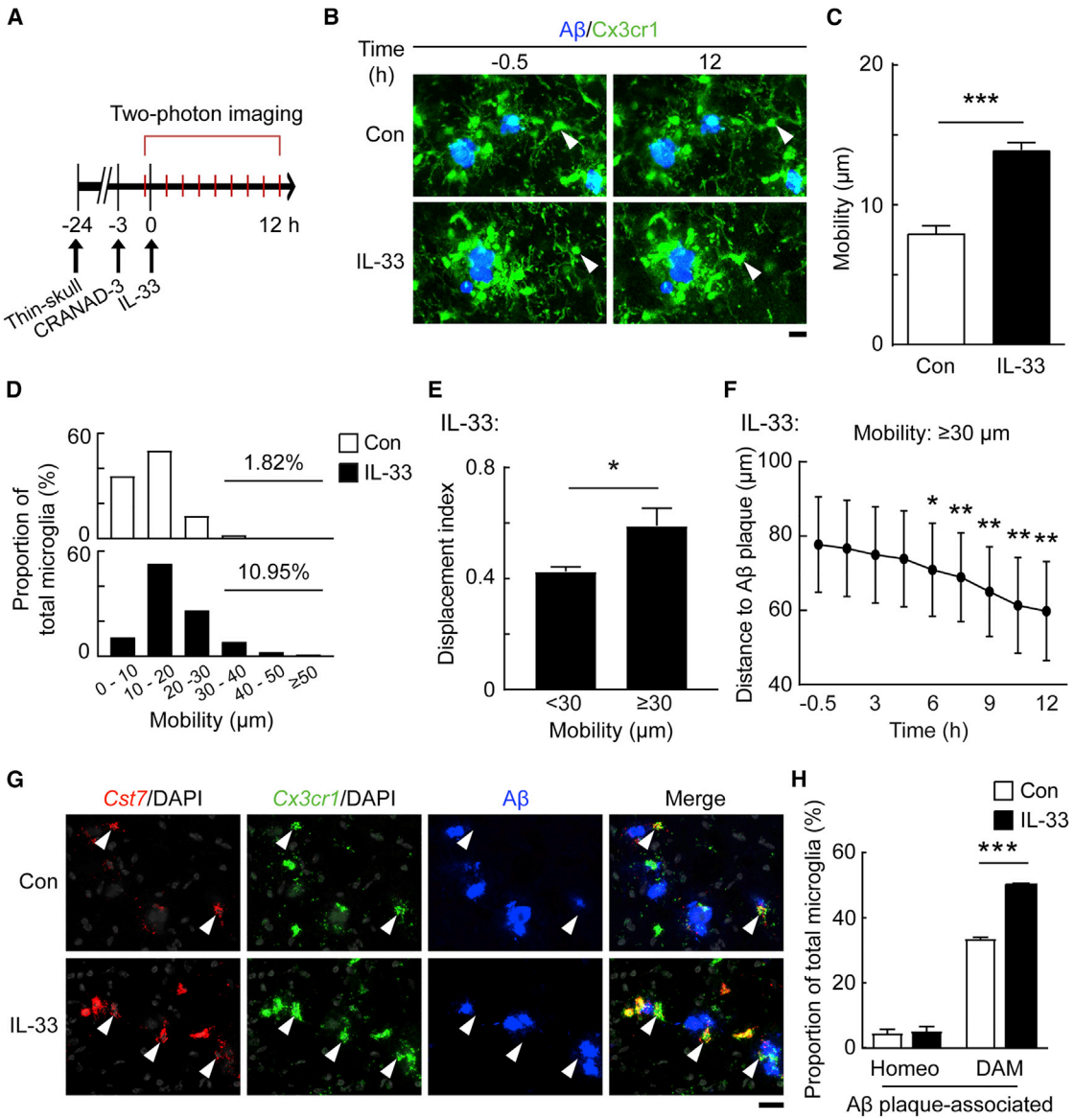

Figure 1. IL-33 Injection Enhances Chemotactic Response of a Specific Microglial Subpopulation in APP/PS1 Mice

(A–F) *In vivo* two-photon imaging of microglia and beta-amyloid (Aβ) plaques in the cortices from APP/PS1;Cx3cr1$^{eYFP/+}$ mice after interleukin (IL)-33 injection.

(A) Schematic diagram of experimental design.

(B–F) IL-33 injection increased microglial chemotaxis toward Aβ plaques.

(B) Representative images showing the interaction between eYFP^{+} microglia and CRANAD-3-labeled Aβ plaques 0.5 h before and 12 h after IL-33 injection. Arrowheads denote the same microglia. Scale bar, 20 μm.

(C) Average distance traveled by microglia in 12 h (Con: n = 110 microglia from three mice; IL-33: n = 274 microglia from four mice; ***p < 0.001 versus Con, Mann-Whitney U test).

(D) Proportion of microglia binarized by mobility over 12 h.

(E) Displacement index of microglia that traveled ≥30 or <30 μm in IL-33-injected APP/PS1 mice. The displacement index was calculated as microglial displacement divided by the distance traveled in 12 h (<30 μm: n = 244 microglia; ≥30 μm: n = 30 microglia from three mice; *p < 0.05 versus <30 μm, Mann-Whitney U test).

(F) Distance between high-mobility microglia (i.e., ≥30-μm migration distance in 12 h) and the nearest Aβ plaques after IL-33 injection (n = 18 microglia from four mice; *p < 0.05; **p < 0.01; ***p < 0.001 versus −0.5 h, repeated-measures one-way ANOVA).

(G and H) IL-33 increased the proportion of DAMs that interacted with 6E10^{+} Aβ plaques in APP/PS1 mice. Representative fluorescence *in situ* hybridization (FISH) images (G) and quantification (H) showing the associations of DAMs (i.e., *Cst7*$^{+}$ *Cx3cr1*$^{+}$ cells) and homeostatic microglia (i.e., *Cst7*$^{-}$ *Cx3cr1*$^{+}$ cells) with 6E10^{+} Aβ plaques in the cortices from APP/PS1 mice 48 h after IL-33 injection (Con: n = 4; IL-33: n = 4; ***p < 0.001 versus Con, Student's t test). Arrowheads denote Aβ-plaque-associated DAMS. Scale bar, 20 μm. All data are presented as mean ± SEM.

See also Figure S1.

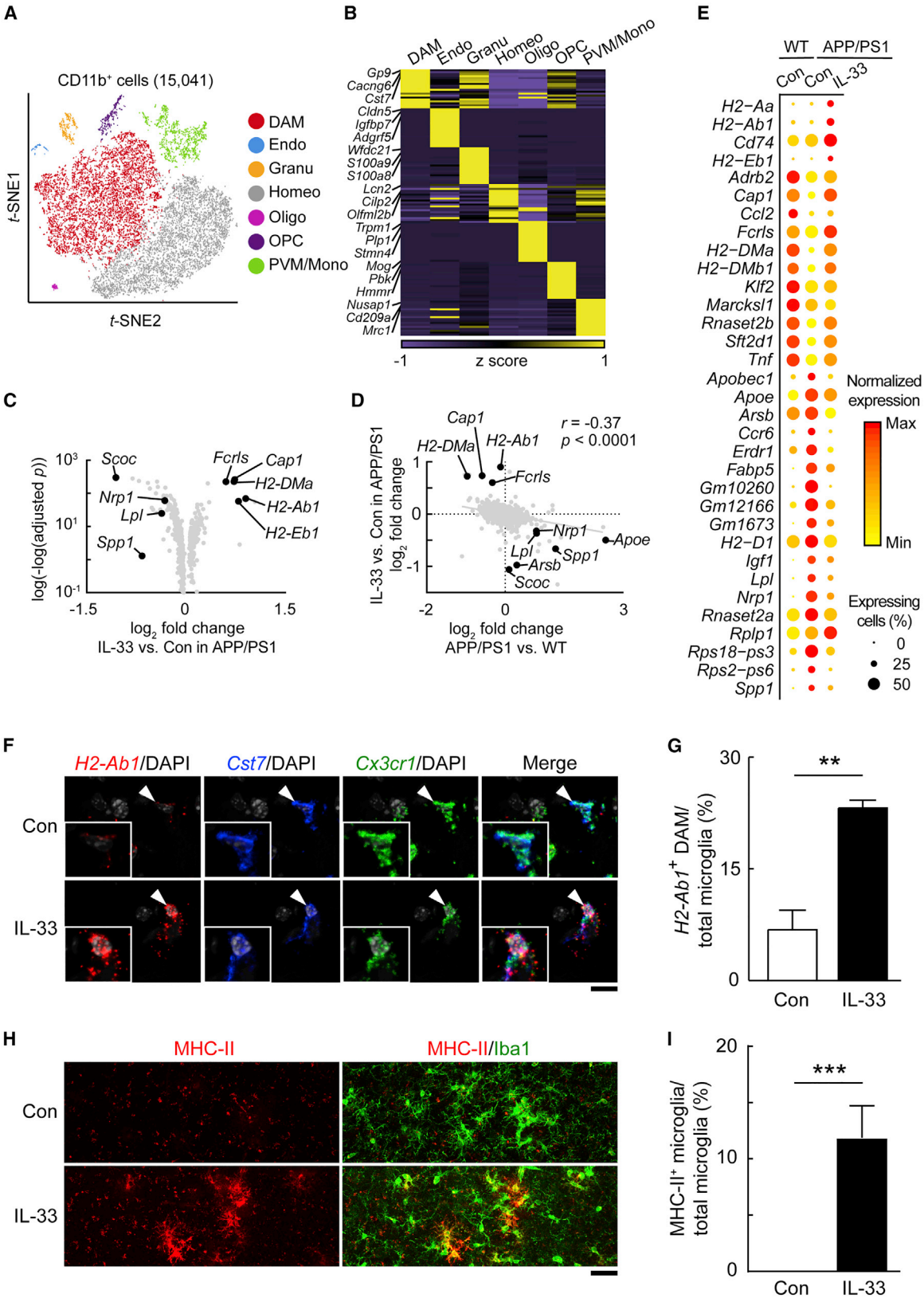

(legend on next page)

To investigate the transcriptome reprogramming in specific microglial subpopulations induced by IL-33, we compared changes in the expression of IL-33-induced DEGs at the single-cell level. Analysis of the expression of homeostatic signature genes (i.e., *Cap1*, *Fcrls*, and *Sft2d1*) showed that IL-33 restored their expression levels in all microglia, including the DAM subpopulation (Figures 2E and S2E). Thus, IL-33 restored the expression of homeostatic signature genes while maintaining the expression of DAM signature genes in the DAM subpopulation. Interestingly, IL-33 specifically induced the expression of MHC-II genes (i.e., *Cd74*, H2-*Ab1*, and *H2-Eb1*) in a DAM subpopulation that co-expressed homeostatic signature genes (Figure S2E), which we termed IL-33RMs. This IL-33RM subpopulation is a transcriptionally distinct microglial subpopulation, when compared to the other MHC-II$^+$ microglia previously reported (Mathys et al., 2017; Sala Frigerio et al., 2019). We then performed multiplex FISH analysis and confirmed that IL-33 injection increased the proportion of *H2-Ab1*$^+$ *Cst7*$^+$ *Cx3cr1*$^+$ microglia (i.e., IL-33RMs) in the cerebral cortex of APP/PS1 mice from 9% to 24% (Figures 2F and 2G). Our immunohistochemical analysis showed that, while only few microglia that express surface MHC-II were found in the cerebral cortex of Con APP/PS1 mice, IL-33 injection significantly increased the proportion of MHC-II$^+$ microglia in the cerebral cortex of APP/PS1 mice by 10% (Figures 2H, 2I, and S2F). As MHC-II is a microglial activation marker (Hopperton et al., 2018), our single-cell transcriptome analysis shows that IL-33RMs represent a subpopulation of activated DAMs that co-expresses homeostatic signature genes.

IL-33RMs Exhibit Enhanced Aβ Phagocytic and Clearance Capacity

Next, we investigated whether IL-33RMs mediate the IL-33-stimulated beneficial outcomes in APP/PS1 mice. We first compared the transcriptome profile of IL-33RMs with that of the MHC-II$^-$ DAMs or homeostatic microglia in these mice following IL-33 injection. The enriched genes in IL-33RMs were associated with angiogenesis (e.g., *Vegfa*), antigen presentation (e.g., *H2-Aa* and *H2-Eb1*), and endocytosis (e.g., *Axl* and *Ctse*) (Figures 3A and 3B), highlighting its role in phagocytic response. The Search Tool for the Retrieval of Interacting Genes/Proteins (STRING) analysis of the genes enriched in IL-33RMs, including *Axl*, *C3*, *Ciita*, *H2-Ab1*, *Ptgs2*, *Spp1*, and *Vefga*, further revealed that they belong to an interconnected gene network that co-regulates pathways highlighted in the Gene Ontology (GO) analysis (Figures 3B and S3A). These highlighted pathways further support the notion that IL-33RMs adopt phenotypes characterized by enhanced chemotaxis and phagocytosis; this is concordant with the function of MHC-II in antigen presentation, in which degraded proteins are presented on the cell surface after phagocytosis (Roche and Furuta, 2015).

Next, we investigated the interaction of IL-33RMs with Aβ plaques in IL-33-injected APP/PS1 mice. Immunohistochemical analysis revealed that most of the IL-33-induced MHC-II$^+$ microglia were associated with Aβ plaques in the cerebral cortex (Figures 3C, 3D, and S3B). Meanwhile, the proportion of Aβ-plaque-associated MHC-II$^-$ microglia remained relatively unchanged in APP/PS1 mice following IL-33 injection (Figures 3C and 3D). To determine whether IL-33RMs mediate Aβ phagocytosis in IL-33-injected APP/PS1 mice, we examined their Aβ uptake *in vivo* by injecting mice with methoxy-X04 (MeX04; a brain penetrant Aβ dye) followed by flow cytometry. In Con APP/PS1 mice, the MHC-II$^+$ microglia only accounted for ~15% of Aβ phagocytic microglia (i.e., MeX04$^+$ CD11b$^+$ cells), whereas IL-33 injection increased the proportion to ~60% (Figures 3E, 3F, S3C, and S3D). Furthermore, in IL-33-injected APP/PS1 mice, the MHC-II$^+$ microglia exhibited increased Aβ phagocytic capacity as indicated by a higher mean fluorescence intensity of MeX04 than

Figure 2. IL-33 Induces a Microglial Subpopulation that Highly Expresses MHC-II and Homeostatic Signature Genes in APP/PS1 Mice

(A–E) scRNA-seq analysis of CD11b$^+$ cells in the forebrain in IL-33-injected APP/PS1 mice. CD11b$^+$ cells were isolated from IL-33-injected APP/PS1 mice, DPBS-injected (Con) APP/PS1 mice, or Con wild-type (WT) mice.

(A and B) Cell-type heterogeneity analysis.

(A) t-Distributed Stochastic Neighbor Embedding (t-SNE) plot showing the seven unique CD11b$^+$ cell clusters (DAM, disease-associated microglia; Endo, endothelial cells; Granu, granulocytes; Homeo, homeostatic microglia; Oligo, oligodendrocytes; OPC, oligodendrocyte precursor cells; PVM/Mono, perivascular macrophages/monocytes) in the CD11b$^+$ cells from IL-33-injected APP/PS1, Con APP/PS1, and WT mice (n = 15,041 cells from three conditions, two mice per condition).

(B) Heatmap showing the top 10 enriched genes in each cell cluster. Gene markers of each cell cluster are listed.

(C–E) IL-33 injection increased the expression of MHC-II and homeostatic signature genes in a microglial subpopulation that co-expressed DAM signature genes in APP/PS1 mice.

(C) Volcano plot showing the differentially expressed genes (DEGs) in microglia (upregulated: 99; downregulated: 141) in IL-33-injected versus Con APP/PS1 mice (Benjamini-Hochberg adjusted $p < 0.1$; $\log_2$ fold change > 0.56 or < -0.56).

(D) Correlations of changes in the microglial transcriptome profiles of IL-33-injected versus Con APP/PS1 mice and APP/PS1 versus WT mice ($r = -0.37$, $p < 0.0001$, linear regression).

(E) Dotplot showing the expression level of the 33 IL-33-induced DEGs including MHC-II genes (i.e., *Cd74*, *H2-Ab1*, and *H2-Eb1*) and homeostatic signature genes (i.e., *Cap1*, *Fcrls*, *H2-DMa*, and *Sft2d1*) in microglia in each condition.

(F–I) Induction of the IL-33RM subpopulation in APP/PS1 mice upon IL-33 injection.

(F) Representative images of FISH analysis for *H2-Ab1* (a MHC-II gene), *Cst7* (a DAM marker), and *Cx3cr1* (a microglial marker) in the cortices from IL-33-injected and Con APP/PS1 mice. Arrowheads denote the DAMs in the insets. Scale bar, 10 μm.

(G) Proportions of *H2-Ab1*$^+$ DAMs (indicated by *Cst7*$^+$ *Cx3cr1*$^+$) in the cortices from IL-33-injected and Con APP/PS1 mice (Con: n = 4; IL-33: n = 4; $^{**}p < 0.01$ versus Con, Student's t test).

(H and I) Representative images (H) and quantification (I) of immunohistochemical analysis for MHC-II and Iba1 (a microglial marker) in the cortices from IL-33-injected and Con APP/PS1 mice (Con: n = 3, IL-33: n = 4; $^{***}p < 0.001$ versus Con, Student's t test). Scale bar = 20 μm. All data are presented as mean ± SEM. See also Figure S2.

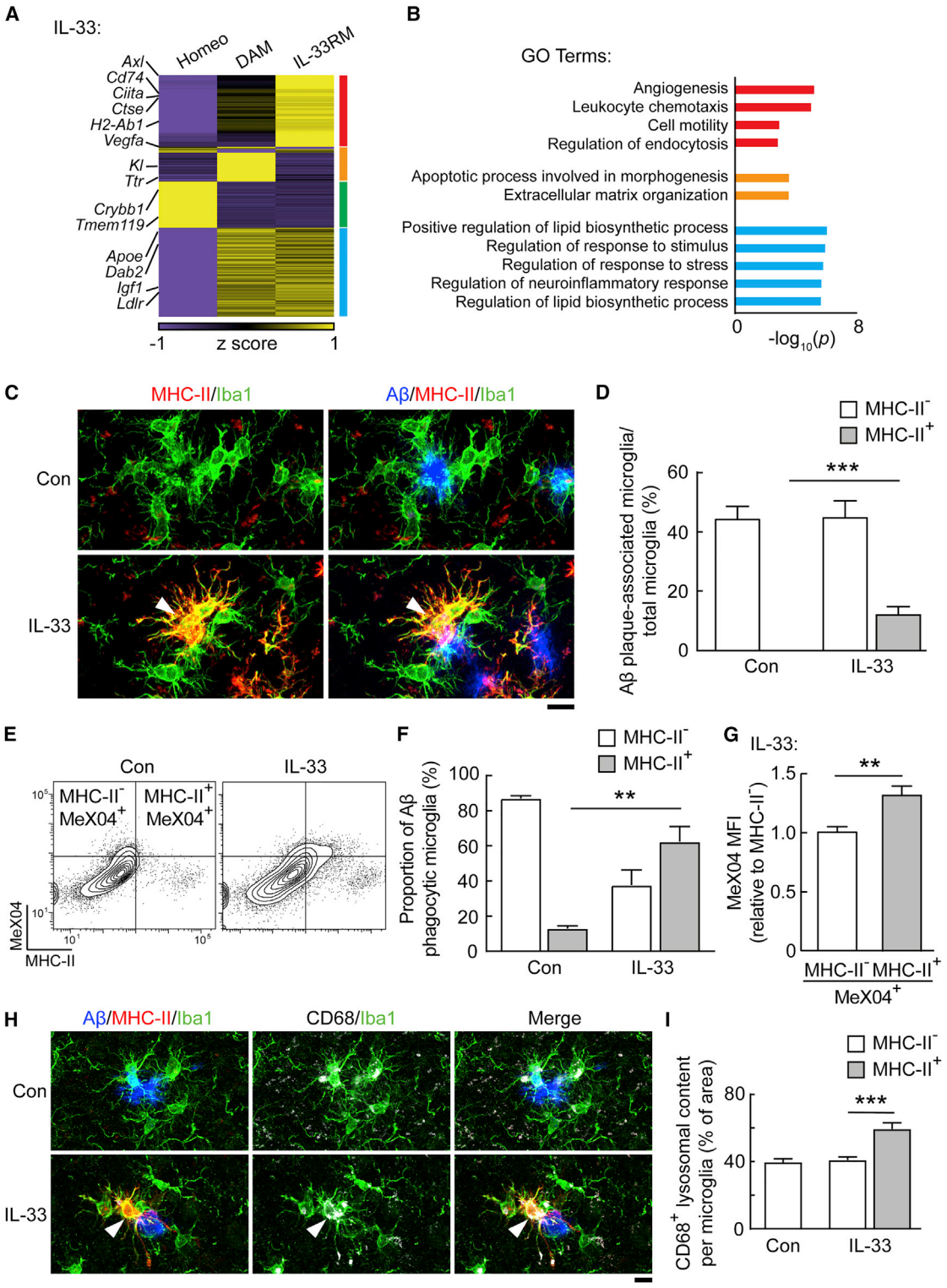

Figure 3. IL-33RMs Possess Enhanced Aβ Clearance Capacity in APP/PS1 Mice

(A and B) Gene clustering analysis shows that IL-33RMs were associated with chemotactic and endocytic pathways.

(A) Heatmap showing the transcriptome profiles of IL-33RMs, DAMs, and homeostatic microglia in IL-33-injected APP/PS1 mice.

(B) Bar plot showing top GO pathways associated with each gene cluster.

(C and D) IL-33RMs were associated with Aβ plaques.

(legend continued on next page)

that in MHC-II$^-$ microglia (Figure 3G). In addition, among the Aβ-plaque-associated microglial subpopulations, MHC-II$^+$ microglia had higher CD68$^+$ lysosomal content than MHC-II$^-$ microglia in both IL-33-injected and Con APP/PS1 mice (Figures 3H, 3I, S3E, and S3F). These findings demonstrate that IL-33RMs possess higher Aβ phagocytic capacity than that of the other microglial subpopulations.

Remodeling of Chromatin Accessibility Regulates the IL-33-Induced Cell State Transition in Microglia

In microglia, the reprogramming of transcriptome profile is regulated by the dynamic modulation of the epigenetic landscape (Cheray and Joseph, 2018; Holtman et al., 2017). To understand how the transcriptome profile of IL-33RMs is shaped, we compared the chromatin accessibility landscape of IL-33RMs with that of the other non-responsive microglia (i.e., MHC-II$^-$ CD11b$^+$ CD45$^+$ cells) in IL-33-treated APP/PS1 mice by using the assay for transposase-accessible chromatin with sequencing (ATAC-seq). In IL-33RMs, we identified 10,775 regions (increased: 6,159; decreased: 4,616) with differential chromatin accessibility (Figure 4A). The Genomic Regions Enrichment of Annotations Tool (GREAT) (McLean et al., 2010) analysis showed that the regions with increased chromatin accessibility were associated with pathways related to macrophage activation and myeloid differentiation (Figure 4B), consistent with their activated phenotypes (Figure 2). Next, we focused our analysis on the signature genes of IL-33RMs (i.e., MHC-II genes) and showed that IL-33RMs have a significantly increased chromatin accessibility at the regulatory regions of MHC-II genes compared to that of the non-responsive microglia (Figures 4C and 4D). Indeed, these regions also showed increased chromatin accessibility in total microglia in IL-33-treated APP/PS1 mice (Figures S4A and S4B). These data together show that the remodeling of chromatin accessibility in microglia correlated with the transcriptome reprogramming upon IL-33 treatment.

To examine how the chromatin-accessible regions of DEGs regulate gene expression, we used chromatin immunoprecipitation sequencing (ChIP-seq) to examine the genome-wide H3K4me3 landscape, which marks active promoter regions (Cedar and Bergman, 2009), in the microglia in IL-33-injected APP/PS1 mice. Comparison of H3K4me3 signal intensity at all transcription start sites, including the regulatory regions of the DEGs (e.g., MHC-II genes), showed that the H3K4me3 landscape in microglia was not changed by IL-33, suggesting that these microglial genes are already permissive for activation in APP/PS1 mice (Figures 4E and S4C). Intriguingly, overlaying the H3K4me3 landscape with the chromatin accessibility landscapes revealed that IL-33 injection increased the chromatin accessibility at the active promoter regions of DEGs (Figures 4F and S4D). Taken together, our results show that IL-33 regulates the chromatin accessibility at the IL-33RM signature genes according to their expression changes during the induction of IL-33RMs.

IL-33 Regulates PU.1 Binding to MHC-II Genes

The modulation of chromatin accessibility at the gene regulatory regions alters the binding affinity of transcription factors (TFs), thus regulating gene transcription (Klemm et al., 2019). To investigate whether and how the IL-33-dependent remodeling of chromatin accessibility regulates the binding of TFs, we first identified the 25,731 genomic regions that are both chromatin accessible and enriched with H3K4me3 marks in microglia in IL-33-injected APP/PS1 mice (Figure 5A). A *de novo* motif search for the TF-binding sites in these sequences showed that they were enriched with the Sfpi1/PU.1 motif (Figure 5B) (Heinz et al., 2010). PU.1 is a myeloid lineage-specific TF that coordinates the transcriptional program during hematopoiesis, antigen presentation, and microglial development (van den Elsen, 2011; Heinz et al., 2015; Kierdorf et al., 2013; Kitamura et al., 2012). To investigate whether IL-33 remodels the PU.1-binding landscape in microglia in APP/PS1 mice, we used ChIP-seq to profile and compare the PU.1-binding landscape in microglia in IL-33-injected and Con APP/PS1 mice. While the binding pattern of PU.1 was largely similar between microglia in IL-33-injected and Con APP/PS1 mice (80,726 overlapping regions), IL-33 injection increased PU.1 binding together with chromatin accessibility at these regions (Figures 5C and 5D). GREAT analysis revealed that these genomic regions with increased PU.1 binding upon IL-33 injection were associated with genes that regulate phagocytosis and filopodium assembly, whereas the regions with reduced PU.1 binding were associated with genes involved in pathways of intrinsic apoptotic signaling and signaling response to DNA damage (Figure S5).

(C) Representative images showing the interactions of MHC-II$^+$ microglia with MeX04$^+$ Aβ plaques in the cortices from IL-33-injected and Con APP/PS1 mice. Arrowheads denote MHC-II$^+$ microglia. Scale bar, 10 μm.

(D) Proportions of MHC-II$^+$ and MHC-II$^-$ microglia that were associated with Aβ plaques in the cortices from IL-33-injected and Con APP/PS1 mice (Con: n = 3; IL-33: n = 4; ***p < 0.001 versus Con, Student's t test).

(E–G) IL-33RMs exhibited enhanced Aβ phagocytic capacity.

(E and F) Representative contour plots (E) and quantification (F) indicate the proportion of Aβ-phagocytic (i.e., MeX04$^+$) MHC-II$^+$ microglia in the forebrains from IL-33-injected and Con APP/PS1 mice (Con: n = 4; IL-33: n = 7; **p < 0.01, Student's t test).

(G) Relative MeX04 mean fluorescence intensity (MFI) of MHC-II$^+$ and MHC-II$^-$ MeX04$^+$ microglia in IL-33-injected APP/PS1 mice (indicating Aβ phagocytic capacity; IL-33: n = 7; **p < 0.01, paired Student's t test).

(H and I) IL-33RMs that were associated with Aβ plaques exhibited enhanced lysosomal activity in IL-33-injected APP/PS1 mice.

(H) Representative images showing the CD68$^+$ lysosomal content in MHC-II$^+$ and MHC-II$^-$ microglia that were associated with Aβ plaques in IL-33-injected and Con APP/PS1 mice. Arrowhead denotes MHC-II$^+$ microglia. Scale bar, 10 μm.

(I) Quantification of CD68$^+$ lysosomal content per microglia, calculated as CD68$^+$ lysosomal area divided by the corresponding Iba1$^+$ microglial area (IL-33: MHC-II$^+$, n = 17 microglia; MHC-II$^-$, n = 65 microglia, from six mice; Con: MHC-II$^-$, n = 50 microglia from eight mice). ***p < 0.001 versus MHC-II$^-$, Mann-Whitney U test). All data are presented as mean ± SEM.

See also Figure S3.

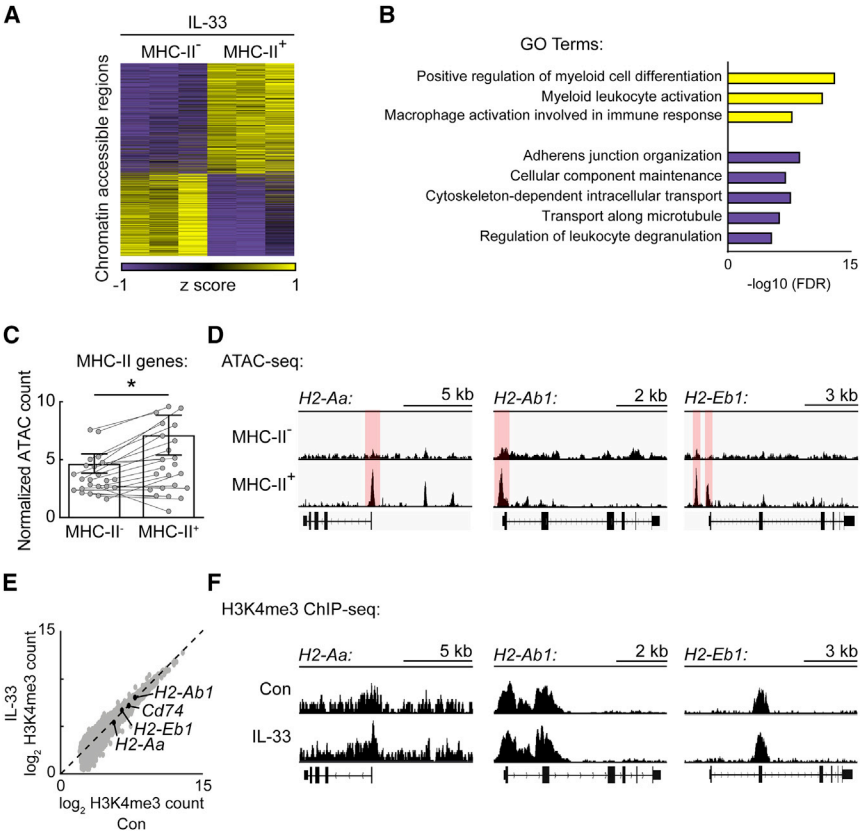

Figure 4. Chromatin Accessibility Landscape Remodeling by IL-33 Is Correlated with the Induction of IL-33RMs in APP/PS1 Mice

(A and B) IL-33RMs exhibit a distinctive chromatin accessibility landscape compared to the non-responsive microglia in IL-33-treated APP/PS1 mice.

(A) Heatmap showing the regions with differential chromatin accessibility (increased: 6,159; decreased: 4,616) in IL-33RMs (i.e., MHC-II$^+$ microglia) ($p < 0.05$).

(B) Highlighted GO pathways from GREAT analysis of the differentially accessible regions are listed.

(C and D) IL-33RMs have increased chromatin accessibility at the regulatory regions of MHC-II genes.

(C) Quantification showing the normalized count of ATAC-seq at the chromatin-accessible regions associated with MHC-II genes (*$p < 0.05$, Student's t test).

(D) Visualization of the chromatin accessibility landscape at the regulatory regions of MHC-II genes (i.e., *H2-Aa*, *H2-Ab1*, and *H2-Eb1*) in IL-33RMs (i.e., MHC-II$^+$ microglia) and non-responsive microglia (i.e., MHC-II$^-$ microglia).

(E and F) IL-33 regulated chromatin accessibility at the active promoter (i.e., H3K4me3-enriched) regions of IL-33 DEGs.

(E) Correlation of the H3K4me3 signal intensity at all H3K4me3-enriched regions between microglia in IL-33-injected and Con APP/PS1 mice. Regulatory regions of MHC-II signature genes are indicated by black dots.

(F) Visualization of the H3K4me3 landscape at the regulatory regions of MHC-II genes (i.e., *H2-Aa*, *H2-Ab1*, and *H2-Eb1*) in microglia in IL-33-injected and Con APP/PS1 mice.

See also Figure S4.

Of note, the changes in PU.1 binding at the regulatory regions of IL-33RM signature genes were positively correlated with their gene expression changes upon IL-33 injection (Figures 2C and 5E). Specifically, for the MHC-II genes (i.e., *Cd74*, *H2-Aa*, *H2-Ab1*, and *H2-Eb1*), IL-33 injection also increased the PU.1 binding at their regulatory regions (Figure 5F). Thus, our data show that IL-33 regulates the binding of the PU.1 transcription factor to IL-33RM signature genes and controls their expression during IL-33RM induction.

PU.1 Activity Is Required for the IL-33-Induced Microglial State Transition and Clearance Activity in AD

To determine how PU.1-depedent transcriptional regulation controls the induction of IL-33RMs and subsequent Aβ clearance in AD, we intracerebroventricularly injected APP/PS1 mice with DB2313, a small-molecule inhibitor that disrupts PU.1-DNA interaction (Antony-Debré et al., 2017), before injecting IL-33. We first examined the effect of PU.1 inhibition on the IL-33-induced reprogramming of the microglial transcriptome by conducting scRNA-seq. Unbiased t-SNE clustering identified different cell clusters, including DAMs and homeostatic microglia, on the basis of cell-type-specific marker genes (Figures 2B and 6A). DB2313 treatment did not significantly alter the proportion of DAMs in IL-33-injected APP/PS1 mice (Figures 6B and 6C) but, interestingly, induced a subset of *KI*$^+$ DAMs (Figure S6A; Table S3). By comparing the changes in the microglial transcriptome, we identified 337 DEGs in IL-33-injected APP/PS1 mice after PU.1 inhibition (Figure 6D). Specifically, PU.1 inhibition downregulated the genes that were upregulated by IL-33 in APP/PS1 microglia, including MHC-II genes (i.e., *Cd74*, *H2-Aa*, *H2-Ab1*, and *H2-Eb1*) and homeostatic signature genes (i.e., *Cap1*, *Sft2d1*, and *Zfp69*) (Figures 6D and S6B). GO analysis further revealed that these downregulated genes were associated with chemotactic responses and antigen presentation, which are, in turn, associated with the functions elicited by IL-33RMs (Figure S6C). At the single-cell level, PU.1 inhibition abolished the induction of the IL-33RM subpopulation by IL-33 (Figure 6E). Furthermore, immunohistochemical staining confirmed that PU.1 inhibition abolished the induction of the IL-33RM subpopulation that associated with Aβ plaques in IL-33-injected APP/PS1 mice (Figures 6F and 6G). Consistently, knockdown of PU.1 by antisense oligonucleotides in the microglial cell line BV2 also attenuated the increased expression of MHC-II genes induced by IL-33 (Figure S6D). Importantly, DB2313 treatment also attenuated the IL-33-induced Aβ clearance in APP/PS1 mice (Figures 6H and 6I). Thus, our findings demonstrate that PU.1-dependent

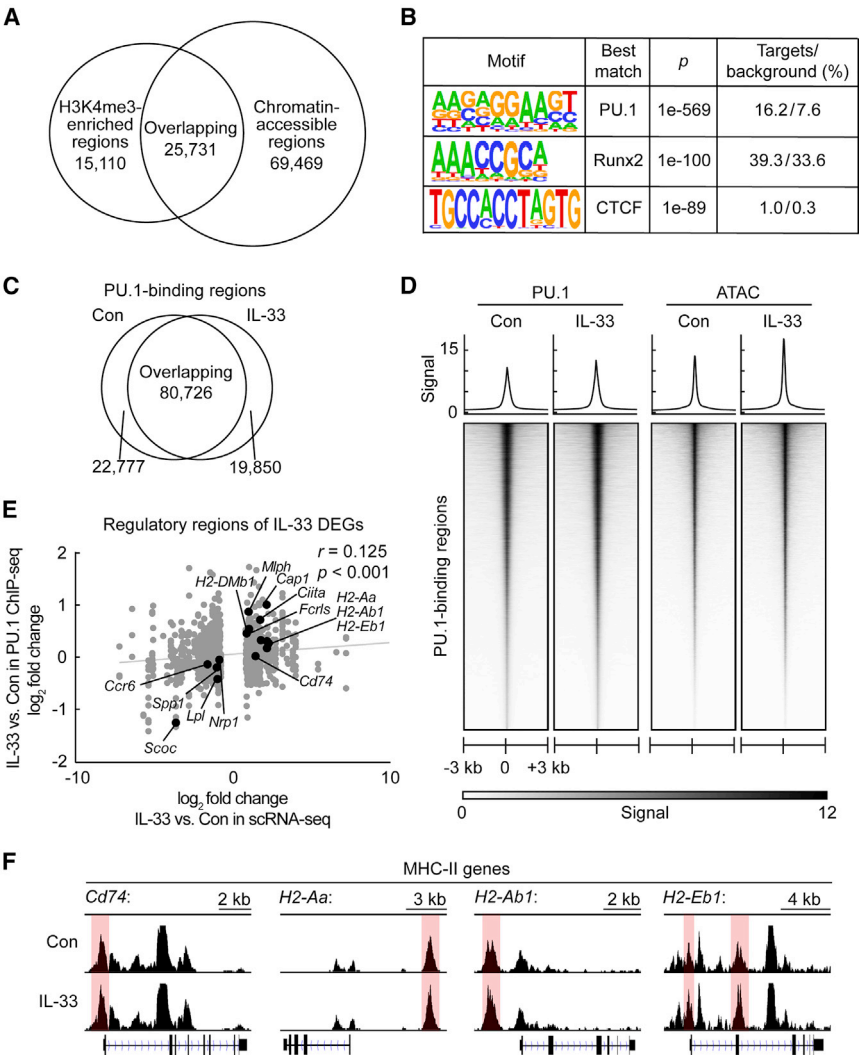

Figure 5. IL-33 Injection Regulates PU.1 Binding to MHC-II Genes in Microglia in APP/PS1 Mice

(A and B) The PU.1-binding motif was enriched in active, chromatin-accessible promoter regions.

(A) Venn diagram showing the overlapping regions between H3K4me3-enriched regions and chromatin-accessible regions in IL-33-injected APP/PS1.

(B) *De novo* motif search of the overlapping regions showing the enrichment of the PU.1 binding motif in these regions.

(C and D) IL-33 injection remodeled the PU.1-binding landscape in microglia in APP/PS1 mice.

(C) Venn diagram showing PU.1-binding regions in microglia in IL-33-injected and Con APP/PS1 mice.

(D) Heatmap of PU.1 chromatin immunoprecipitation sequencing (ChIP-seq) and ATAC-seq signals at the regions ± 3 kb from the overlapping PU.1-binding regions in microglia in IL-33-injected and Con APP/PS1 mice.

(E and F) IL-33 injection remodeled PU.1 binding at the regulatory regions of IL-33RM signature genes, including MHC-II genes.

(E) Correlations of changes in PU.1 binding at the regulatory regions of IL-33 DEGs with the corresponding expression changes in microglia upon IL-33 injection ($r = 0.125$, $p < 0.001$, linear regression). Target genes are indicated by black dots.

(F) Visualization of the PU.1-binding landscape at the regulatory regions of MHC-II genes (i.e., *Cd74*, *H2-Aa*, *H2-Ab1*, and *H2-Eb1*) in microglia in IL-33-injected and Con APP/PS1 mice. Regions with increased PU.1 binding upon IL-33 injection are highlighted in red.

See also Figure S5.

transcriptional reprogramming and functional remodeling of microglia mediate Aβ clearance upon IL-33 injection in AD.

DISCUSSION

The present study reveals an IL-33-PU.1 pathway of epigenetic control in regulating the microglial transcriptome to induce a microglial subpopulation for enhanced Aβ clearance. The induction of the IL-33RM subpopulation is controlled through regulating chromatin accessibility and binding the PU.1 transcription factor of its signature genes upon IL-33 injection. This PU.1-dependent transcriptome reprogramming is critical for the IL-33-stimulated Aβ clearance. To our knowledge, this study is the first to demonstrate the enhancement of Aβ clearance through reprogramming the epigenetic and transcriptomic profiles of a microglial subpopulation, leading to the amelioration of AD pathology.

Transcriptome profiling of the IL-33RM subpopulation reveals that they express a unique transcriptome signature highlighted by the co-expression of DAM signature genes, homeostatic signature genes, and MHC-II genes, indicating that IL-33RMs represent a distinct subset of activated DAMs (Keren-Shaul et al., 2017; Sala Frigerio et al., 2019). Although the roles of DAMs in AD remain controversial, studies have suggested that DAMs exhibit differential phenotypes and functional properties along AD progression. Specifically, the induction of DAMs at the early stage of AD is beneficial to Aβ pathology but becomes detrimental upon disease progression (Deczkowska et al., 2018; Jay et al., 2015; Parhizkar et al., 2019). The regulation of the DAM transcriptome program along AD progression might reflect their functional modulation. At the early AD stage, the DAM induction is concomitant with a reduced expression of homeostatic signature genes, including purine receptor (*P2ry12* and *P2ry13*), Fc receptor (*Fcrls*), and cytoskeletal-remodeling proteins (*Cap1*) (Butovsky et al., 2014; Keren-Shaul et al., 2017; Krasemann et al., 2017). Meanwhile, at the later stage of AD, genes encoding cell-adhesion molecules (e.g., *Itgax*) as well as genes involved in phagocytosis (*Cst7*) and lipid metabolism (*Lpl* and *Spp1*) are induced in DAMs (Kamphuis et al., 2016; Keren-Shaul et al.,

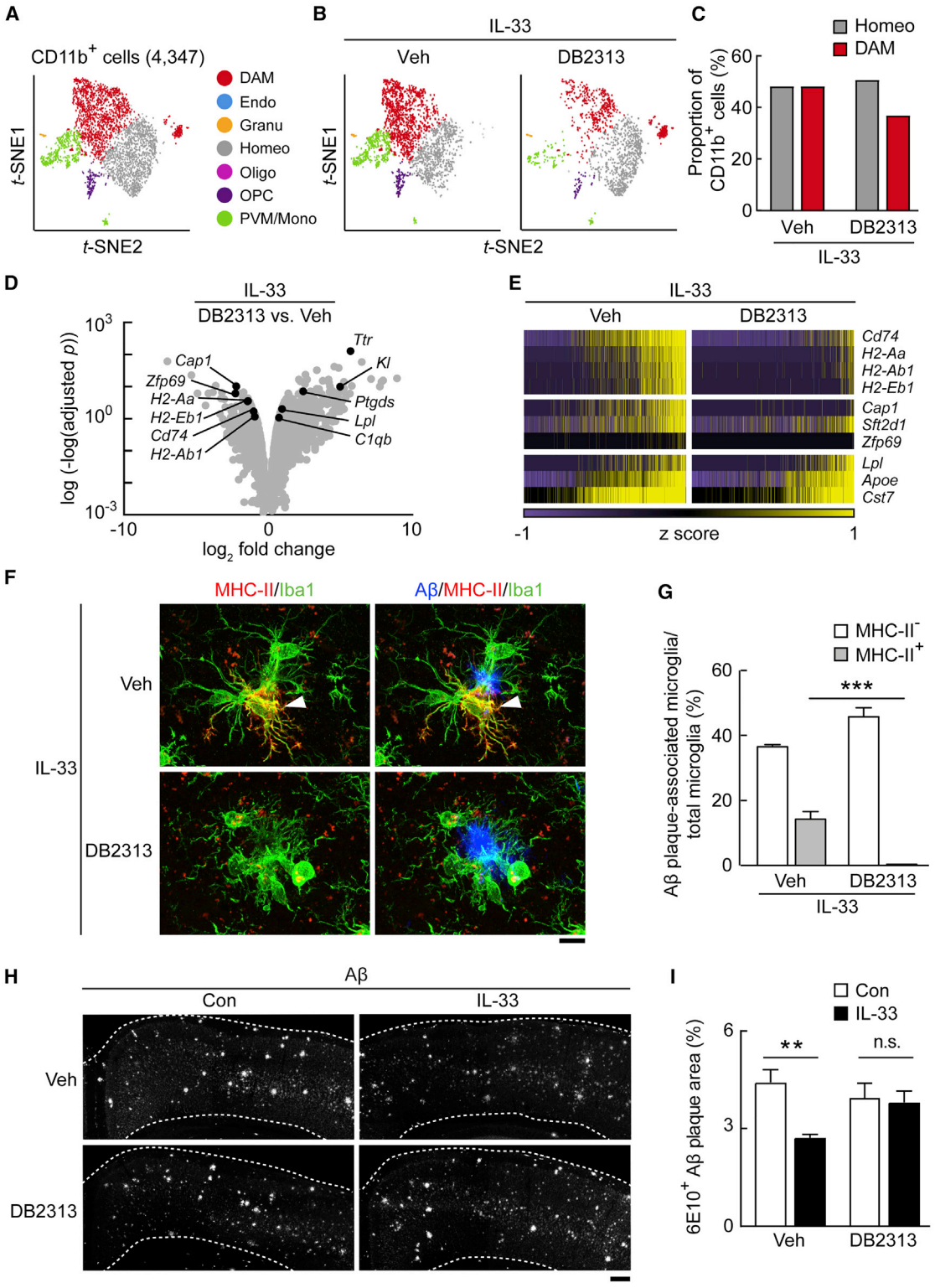

Figure 6. The PU.1-Dependent Induction of IL-33RMs Is Required for IL-33-Stimulated Aβ Clearance in APP/PS1 Mice

(A–E) PU.1 inhibition abolished the microglial state transition in APP/PS1 mice upon IL-33 injection. APP/PS1 mice were intracerebroventricularly administered DB2313 (a small molecule inhibitor of PU.1) or artificial cerebrospinal fluid (Veh), followed by IL-33 injection 24 h later.

(A) t-SNE plot showing cell type heterogeneity.

(legend continued on next page)

2017; Nishitsuji et al., 2011). Interestingly, IL-33 injection reduces the expression of DAM signature genes that are induced at the later stage of AD (i.e., *Itgax*, *Lpl*, and *Spp1*) and restores the expression of homeostatic signature genes (i.e., *Cap1* and *Fcrls*) in IL-33RMs. Moreover, IL-33RMs recapitulate the enhanced Aβ clearance activity of "early-stage DAMs," suggesting that they transcriptionally and functionally resemble the early-stage DAMs. Detailed studies on the functional roles of different microglial signatures will decipher the molecular mechanisms that control the clearance activity of microglia in AD as well as other neurodegenerative diseases.

Besides regulating the transcriptome changes in microglia along AD progression, IL-33 injection specifically induces MHC-II complexes in the IL-33RM subpopulation. In myeloid cells, surface expression of MCH-II represents the end stage of antigen presentation, a process in which exogenous proteins are phagocytosed and the digested peptides are presented onto the MHC-II machinery (Cella et al., 1997; Roche and Furuta, 2015). Indeed, our transcriptome analysis shows that this microglial subpopulation is enriched with the full spectrum of genes involved in the machinery for antigen processing and presentation, including genes associated with vesicle transport (i.e., homeostatic signature genes including *Cap1*, *Mlph*, and *Sft2d1*) (Lee et al., 2014; Matesic et al., 2001; Trost et al., 2009; Zhang et al., 2013), non-classical MHC-II (e.g., *H2-DMa* and *H2-DMb1*) (Alfonso and Karlsson, 2000; Mellins and Stern, 2014), and the MHC-II complex itself (e.g., *H2-Ab1* and *H2-Eb1*). This suggests that MHC-II$^+$ IL-33RMs can degrade phagocytosed Aβ. Furthermore, a recent study revealed that global ablation of MHC-II exaggerates Aβ pathology in an AD mouse model (Mittal et al., 2019), highlighting the involvement of MHC-II in Aβ clearance by microglia. Thus, the MHC-II complex might play an important role in the enhanced Aβ clearance activity of IL-33RMs. Given that MHC-II is induced in microglia of AD patients as well as mouse models of various neurodegenerative diseases (Masuda et al., 2019; Mathys et al., 2017; Perlmutter et al., 1992; Sala Frigerio et al., 2019), investigating the molecular and functional characteristics of the MHC-II$^+$ microglia in AD patient may provide insights into their roles along AD progression.

The induction of IL-33RMs depends on the microglial state transition induced by IL-33, an endogenous cytokine found in the brain that functions as an alarmin to stimulate the recruitment of microglia upon injury (Gadani et al., 2015). The action of IL-33 is triggered by binding to its receptor, the growth stimulation expressed gene 2 (ST2) (Cayrol and Girard, 2014; Schmitz et al., 2005). We recently found that a subpopulation of microglia expresses higher ST2 levels in both AD patients and AD transgenic mice (unpublished data). Therefore, injecting IL-33 might stimulate the microglial state transition and, subsequently, enhance Aβ clearance activity through activation of the ST2 signaling in microglia. The expression of ST2 is regulated in different cellular injury conditions, either through the negative-feedback mechanism triggered by IL-33 or through the alteration of the proteasomal-dependent degradation pathway (Ciechanover and Kwon, 2015; Gadani et al., 2015; Zhao et al., 2012). Indeed, perturbed activation of ST2 signaling, marked by reduced IL-33 transcript levels and increased levels of the decoy receptor, soluble ST2, is observed in patients with AD or mild cognitive impairment (Chapuis et al., 2009; Fu et al., 2016). Thus, it is of interest to investigate the molecular mechanism that controls ST2 induction in microglia and the dysregulation of IL-33/ST2 signaling during the onset/progression of AD.

How does activation of ST2 signaling lead to state transition of microglia? In healthy and diseased conditions, the state transition of microglia is controlled through transcriptome reprogramming fine-tuned by the remodeling of the chromatin state (Cheray and Joseph, 2018; Yeh and Ikezu, 2019). Therefore, chromatin state remodeling is a critical epigenetic control for the active transition of the microglial state (Ayata et al., 2018; Datta et al., 2018). Although epigenetic control during microglial development has been extensively investigated (Kierdorf and Prinz, 2013; Kierdorf et al., 2013; Matcovitch-Natan et al., 2016), it is unclear how microglial activation is regulated by epigenetic remodeling in AD. In the present study, we show that, during the IL-33-induced state transition of microglia, the remodeling of chromatin accessibility regulates PU.1 binding at IL-33RM signature genes and, thus, controls their gene transcription. Importantly, this IL-33-induced remodeling of the PU.1-binding landscape is required for the IL-33-induced transcriptome reprogramming and state transition of microglia in AD transgenic mice. PU.1 is a key transcription regulator of microglial state during differentiation and maturation (Kierdorf and Prinz, 2013; Kierdorf et al., 2013). A recent study highlighted that genetic variants of *PU.1* are associated with the onset age of AD and the reduced *PU.1* expression in myeloid cells (Huang et al., 2017). Thus, understanding the PU.1-dependent transcriptional control of microglial state transition may provide insights into the development of therapeutic approaches for AD.

(B) t-SNE plots showing the CD11b$^+$ cell clusters in DB2313- or Veh-injected APP/PS1 mice (DB2313: n = 1,629 cells; Veh: n = 2,718 cells).
(C) Bar plot showing the proportions of DAMs and homeostatic microglia in DB2313- and Veh-injected APP/PS1 mice in the presence of IL-33. (D and E) PU.1 inhibition abolished the induction of MHC-II genes and homeostatic signature genes in microglia in APP/PS1 mice upon IL-33 injection.
(D) Volcano plot showing the DEGs (upregulated: 248; downregulated: 88) in APP/PS1 mouse microglia after IL-33 injection with or without DB2313 administration (Benjamini-Hochberg adjusted $p < 0.1$; $\log_2$ fold change > 0.56 or < -0.56).
(E) Heatmap showing the expression of MHC-II genes (i.e., *Cd74*, *H2-Aa*, H2-*Ab1*, and *H2-Eb1*), homeostatic signature genes (i.e., *Cap1*, *Sft2d1*, and *Zfp69*), and DAM signature genes (i.e., *Apoe*, *Cst7*, and *Lpl*) in microglia in both conditions.
(F and G) PU.1 inhibition abolished the induction of IL-33RMs, which were associated with Aβ plaques, upon IL-33 injection. Representative images (F) and quantification (G) of Aβ-plaque-associated IL-33RMs in the cortices from DB2313- or Veh-injected APP/PS1 mice after IL-33 injection (Veh: n = 3; DB2313: n = 4; ***$p < 0.001$ versus Veh, Student's t test). Arrowheads denote MHC-II$^+$ microglia. Scale bar, 10 μm.
(H and I) PU.1 inhibition attenuated the IL-33-stimulated decrease of Aβ deposition in APP/PS1 mice. Representative images (H) and quantification (I) of 6E10$^+$ Aβ plaques in the cortices from DB2313- or Veh-injected APP/PS1 mice after IL-33 injection (for Con: Veh, n = 7; DB2313, n = 7; for IL-33: Veh, n = 7; DB2313, n = 7; **$p < 0.01$; n.s. = not significant, two-way ANOVA). Scale bar, 200 μm. All data are presented as mean ± SEM.
See also Figure S6.

Nonetheless, an intriguing question remains: how does IL-33 precisely remodel the chromatin state at the regulatory regions of IL-33RM signature genes? We hypothesized that the specificity of chromatin remodeling is determined by IL-33 signal-dependent TFs such as nuclear factor κBs (NF-κBs) (Carriere et al., 2007). Activation of NF-κBs by IL-33/ST2 signaling triggers the nuclear translocation of the NF-κBs (Schmitz et al., 2005). Once inside the nucleus, NF-κBs can bind to genomic regions containing their binding motifs and further recruit nucleosome-remodeling proteins to modify the chromatin accessibility at these regions (Sima et al., 2018). Therefore, it would be interesting to determine how IL-33 signal-dependent TFs recruit nucleosome-remodeling proteins to remodel the chromatin accessibility landscape in microglia and thus facilitate PU.1 binding. Furthermore, given the ability of PU.1 to interact with other TFs to regulate transcriptome profiling in microglia (Glass and Natoli, 2016; Heinz et al., 2010), PU.1 might function with other TFs downstream of IL-33 to control the induction of IL-33RMs.

Although there is currently no effective therapy for AD, the past decade of AD research has demonstrated that innate immunity plays a pivotal role in AD pathogenesis. While transcriptional reprogramming of microglia and their impaired clearance activity is believed to contribute to the disease pathology, it remains unclear whether and how regulation of the microglial state can alleviate AD pathology. Our study demonstrates that the IL-33-PU.1 pathway enhances the Aβ clearance activity of the DAM subpopulation through remodeling of its epigenetic landscape and PU.1 transcriptional control. Thus, our findings provide new insights into the AD therapeutic potential of modulating microglial functional state by reprogramming their epigenetic and transcriptome profile.

STAR★METHODS

Detailed methods are provided in the online version of this paper and include the following:

- KEY RESOURCES TABLE
- RESOURCE AVAILABILITY
  - Lead Contact
  - Materials Availability
  - Data and Code Availability
- EXPERIMENTAL MODEL AND SUBJECT DETAILS
- METHOD DETAILS
  - Reagents
  - *In vivo* experiments
  - *In vivo* two-photon imaging of microglia
  - *In situ* hybridization by RNAscope
  - Flow cytometry and fluorescence-activated cell sorting
  - scRNA-seq library preparation
  - scRNA-seq analysis
  - Immunohistochemistry
  - ATAC-seq library preparation
  - ChIP-seq library preparation
  - ATAC-seq and ChIP-seq analyses
  - PU.1 knockdown in BV2 cells by antisense oligonucleotides
- QUANTIFICATION AND STATISTICAL ANALYSIS

SUPPLEMENTAL INFORMATION

Supplemental Information can be found online at https://doi.org/10.1016/j.celrep.2020.107530.

ACKNOWLEDGMENTS

We thank Ambrose Lam, Angelie Shui, Fion Chuang, Vicky Chau, Li Ouyang, Kit Cheung, Cara Kwong, Dr. Caleb Lui, Dr. Jackie Lau, and Dr. Brian P. Leung for their excellent technical assistance, as well as other members of the Ip laboratory for many helpful discussions. This study was supported in part by the Areas of Excellence Scheme of the University Grants Committee (AoE/M-604/16); the National Key R&D Program of China (2017YFE0190000 and 2018YFE0203600); the Research Grants Council of Hong Kong (the Collaborative Research Fund [C6003-14G], the Theme-Based Research Scheme [T13-605/18W], and the General Research Fund [HKUST16100418 and HKUST16103017]); the Innovation and Technology Commission (ITCPD/17-9); the Guangdong Provincial Key S&T Program (2018B030336001); and the Shenzhen Knowledge Innovation Program (JCYJ20180507183642005 and JCYJ20170413173717055). S.-F.L. is a recipient of the Hong Kong PhD Fellowship Award.

AUTHOR CONTRIBUTIONS

S.-F.L., A.K.Y.F., and N.Y.I. conceived of the project and designed the experiments; S.-F.L. performed most of the experiments; C.C. performed two-photon microscopy experiments; J.Y.Q., T.H.C., and N.Y.I. contributed new reagents/analytic tools; S.-F.L., C.C., W.-Y.F., T.H.C., A.K.Y.F., and N.Y.I. analyzed the data; and S.-F.L., A.K.Y.F., and N.Y.I. wrote the manuscript.

DECLARATION OF INTERESTS

The authors declare no competing interests.

Received: August 16, 2019
Revised: February 11, 2020
Accepted: March 27, 2020
Published: April 21, 2020

REFERENCES

Alfonso, C., and Karlsson, L. (2000). Nonclassical MHC class II molecules. Annu. Rev. Immunol. *18*, 113–142.

Antony-Debré, I., Paul, A., Leite, J., Mitchell, K., Kim, H.M., Carvajal, L.A., Todorova, T.I., Huang, K., Kumar, A., Farahat, A.A., et al. (2017). Pharmacological inhibition of the transcription factor PU.1 in leukemia. J. Clin. Invest. *127*, 4297–4313.

Ayata, P., Badimon, A., Strasburger, H.J., Duff, M.K., Montgomery, S.E., Loh, Y.E., Ebert, A., Pimenova, A.A., Ramirez, B.R., Chan, A.T., et al. (2018). Epigenetic regulation of brain region-specific microglia clearance activity. Nat. Neurosci. *21*, 1049–1060.

Buenrostro, J.D., Giresi, P.G., Zaba, L.C., Chang, H.Y., and Greenleaf, W.J. (2013). Transposition of native chromatin for fast and sensitive epigenomic profiling of open chromatin, DNA-binding proteins and nucleosome position. Nat. Methods *10*, 1213–1218.

Butler, A., Hoffman, P., Smibert, P., Papalexi, E., and Satija, R. (2018). Integrating single-cell transcriptomic data across different conditions, technologies, and species. Nat. Biotechnol. *36*, 411–420.

Butovsky, O., Jedrychowski, M.P., Moore, C.S., Cialic, R., Lanser, A.J., Gabriely, G., Koeglsperger, T., Dake, B., Wu, P.M., Doykan, C.E., et al. (2014). Identification of a unique TGF-β-dependent molecular and functional signature in microglia. Nat. Neurosci. *17*, 131–143.

Carriere, V., Roussel, L., Ortega, N., Lacorre, D.-A., Americh, L., Aguilar, L., Bouche, G., and Girard, J.-P. (2007). IL-33, the IL-1-like cytokine ligand for

ST2 receptor, is a chromatin-associated nuclear factor in vivo. Proc. Natl. Acad. Sci. USA *104*, 282–287.

Cayrol, C., and Girard, J.-P. (2014). IL-33: an alarmin cytokine with crucial roles in innate immunity, inflammation and allergy. Curr. Opin. Immunol. *31*, 31–37.

Cedar, H., and Bergman, Y. (2009). Linking DNA methylation and histone modification: patterns and paradigms. Nat. Rev. Genet. *10*, 295–304.

Celada, A., Borràs, F.E., Soler, C., Lloberas, J., Klemsz, M., van Beveren, C., McKercher, S., and Maki, R.A. (1996). The transcription factor PU.1 is involved in macrophage proliferation. J. Exp. Med. *184*, 61–69.

Cella, M., Sallusto, F., and Lanzavecchia, A. (1997). Origin, maturation and antigen presenting function of dendritic cells. Curr. Opin. Immunol. *9*, 10–16.

Chapuis, J., Hot, D., Hansmannel, F., Kerdraon, O., Ferreira, S., Hubans, C., Maurage, C.A., Huot, L., Bensemain, F., Laumet, G., et al. (2009). Transcriptomic and genetic studies identify IL-33 as a candidate gene for Alzheimer's disease. Mol. Psychiatry *14*, 1004–1016.

Chen, C., Liang, Z., Zhou, B., Li, X., Lui, C., Ip, N.Y., and Qu, J.Y. (2018). *In Vivo* Near-Infrared Two-Photon Imaging of Amyloid Plaques in Deep Brain of Alzheimer's Disease Mouse Model. ACS Chem. Neurosci. *9*, 3128–3136.

Cheray, M., and Joseph, B. (2018). Epigenetics Control Microglia Plasticity. Front. Cell. Neurosci. *12*, 243.

Ciechanover, A., and Kwon, Y.T. (2015). Degradation of misfolded proteins in neurodegenerative diseases: therapeutic targets and strategies. Exp. Mol. Med. *47*, e147.

Condello, C., Yuan, P., Schain, A., and Grutzendler, J. (2015). Microglia constitute a barrier that prevents neurotoxic protofibrillar Aβ42 hotspots around plaques. Nat. Commun. *6*, 6176.

Crotti, A., and Ransohoff, R.M. (2016). Microglial Physiology and Pathophysiology: Insights from Genome-wide Transcriptional Profiling. Immunity *44*, 505–515.

Datta, M., Staszewski, O., Raschi, E., Frosch, M., Hagemeyer, N., Tay, T.L., Blank, T., Kreutzfeldt, M., Merkler, D., Ziegler-Waldkirch, S., et al. (2018). Histone Deacetylases 1 and 2 Regulate Microglia Function during Development, Homeostasis, and Neurodegeneration in a Context-Dependent Manner. Immunity *48*, 514–529.

Deczkowska, A., Keren-Shaul, H., Weiner, A., Colonna, M., Schwartz, M., and Amit, I. (2018). Disease-Associated Microglia: A Universal Immune Sensor of Neurodegeneration. Cell *173*, 1073–1081.

DiSabato, D.J., Quan, N., and Godbout, J.P. (2016). Neuroinflammation: the devil is in the details. J. Neurochem. *139* (*Suppl 2*), 136–153.

Fourgeaud, L., Través, P.G., Tufail, Y., Leal-Bailey, H., Lew, E.D., Burrola, P.G., Callaway, P., Zagórska, A., Rothlin, C.V., Nimmerjahn, A., and Lemke, G. (2016). TAM receptors regulate multiple features of microglial physiology. Nature *532*, 240–244.

Fu, A.K.Y., Hung, K.W., Yuen, M.Y.F., Zhou, X., Mak, D.S.Y., Chan, I.C.W., Cheung, T.H., Zhang, B., Fu, W.-Y., Liew, F.Y., and Ip, N.Y. (2016). IL-33 ameliorates Alzheimer's disease-like pathology and cognitive decline. Proc. Natl. Acad. Sci. USA *113*, E2705–E2713.

Gadani, S.P., Walsh, J.T., Smirnov, I., Zheng, J., and Kipnis, J. (2015). The Glia-Derived Alarmin IL-33 Orchestrates the Immune Response and Promotes Recovery following CNS Injury. Neuron *85*, 703–709.

Glass, C.K., and Natoli, G. (2016). Molecular control of activation and priming in macrophages. Nat. Immunol. *17*, 26–33.

Guillot-Sestier, M.V., Doty, K.R., Gate, D., Rodriguez, J., Jr., Leung, B.P., Rezai-Zadeh, K., and Town, T. (2015). Il10 deficiency rebalances innate immunity to mitigate Alzheimer-like pathology. Neuron *85*, 534–548.

Hansen, D.V., Hanson, J.E., and Sheng, M. (2018). Microglia in Alzheimer's disease. J. Cell Biol. *217*, 459–472.

Heinz, S., Benner, C., Spann, N., Bertolino, E., Lin, Y.C., Laslo, P., Cheng, J.X., Murre, C., Singh, H., and Glass, C.K. (2010). Simple combinations of lineage-determining transcription factors prime *cis*-regulatory elements required for macrophage and B cell identities. Mol. Cell *38*, 576–589.

Heinz, S., Romanoski, C.E., Benner, C., and Glass, C.K. (2015). The selection and function of cell type-specific enhancers. Nat. Rev. Mol. Cell Biol. *16*, 144–154.

Heneka, M.T., Kummer, M.P., Stutz, A., Delekate, A., Schwartz, S., Vieira-Saecker, A., Griep, A., Axt, D., Remus, A., Tzeng, T.C., et al. (2013). NLRP3 is activated in Alzheimer's disease and contributes to pathology in APP/PS1 mice. Nature *493*, 674–678.

Heneka, M.T., Golenbock, D.T., and Latz, E. (2015). Innate immunity in Alzheimer's disease. Nat. Immunol. *16*, 229–236.

Hickman, S.E., Kingery, N.D., Ohsumi, T.K., Borowsky, M.L., Wang, L.C., Means, T.K., and El Khoury, J. (2013). The microglial sensome revealed by direct RNA sequencing. Nat. Neurosci. *16*, 1896–1905.

Holtman, I.R., Skola, D., and Glass, C.K. (2017). Transcriptional control of microglia phenotypes in health and disease. J. Clin. Invest. *127*, 3220–3229.

Hopperton, K.E., Mohammad, D., Trépanier, M.O., Giuliano, V., and Bazinet, R.P. (2018). Markers of microglia in post-mortem brain samples from patients with Alzheimer's disease: a systematic review. Mol. Psychiatry *23*, 177–198.

Huang, K.L., Marcora, E., Pimenova, A.A., Di Narzo, A.F., Kapoor, M., Jin, S.C., Harari, O., Bertelsen, S., Fairfax, B.P., Czajkowski, J., et al. (2017). A common haplotype lowers PU.1 expression in myeloid cells and delays onset of Alzheimer's disease. Nat. Neurosci. *20*, 1052–1061.

Jay, T.R., Miller, C.M., Cheng, P.J., Graham, L.C., Bemiller, S., Broihier, M.L., Xu, G., Margevicius, D., Karlo, J.C., Sousa, G.L., et al. (2015). TREM2 deficiency eliminates TREM2+ inflammatory macrophages and ameliorates pathology in Alzheimer's disease mouse models. J. Exp. Med. *212*, 287–295.

Kamphuis, W., Kooijman, L., Schetters, S., Orre, M., and Hol, E.M. (2016). Transcriptional profiling of CD11c-positive microglia accumulating around amyloid plaques in a mouse model for Alzheimer's disease. Biochim. Biophys. Acta. *1862*, 1847–1860.

Kang, S.S., Ebbert, M.T.W., Baker, K.E., Cook, C., Wang, X., Sens, J.P., Kocher, J.-P., Petrucelli, L., and Fryer, J.D. (2018). Microglial translational profiling reveals a convergent APOE pathway from aging, amyloid, and tau. J. Exp. Med. *215*, 2235–2245.

Keren-Shaul, H., Spinrad, A., Weiner, A., Matcovitch-Natan, O., Dvir-Szternfeld, R., Ulland, T.K., David, E., Baruch, K., Lara-Astaiso, D., Toth, B., et al. (2017). A Unique Microglia Type Associated with Restricting Development of Alzheimer's Disease. Cell *169*, 1276–1290.e17.

Kierdorf, K., and Prinz, M. (2013). Factors regulating microglia activation. Front. Cell. Neurosci. *7*, 44.

Kierdorf, K., Erny, D., Goldmann, T., Sander, V., Schulz, C., Perdiguero, E.G., Wieghofer, P., Heinrich, A., Riemke, P., Hölscher, C., et al. (2013). Microglia emerge from erythromyeloid precursors via Pu.1-and Irf8-dependent pathways. Nat. Neurosci. *16*, 273–280.

Kim, J., Basak, J.M., and Holtzman, D.M. (2009). The role of apolipoprotein E in Alzheimer's disease. Neuron *63*, 287–303.

Kitamura, N., Yokoyama, H., Yashiro, T., Nakano, N., Nishiyama, M., Kanada, S., Fukai, T., Hara, M., Ikeda, S., Ogawa, H., et al. (2012). Role of PU.1 in MHC class II expression through transcriptional regulation of class II transactivator pI in dendritic cells. J. Allergy Clin. Immunol. *129*, 814–824.e6.

Klemm, S.L., Shipony, Z., and Greenleaf, W.J. (2019). Chromatin accessibility and the regulatory epigenome. Nat. Rev. Genet. *20*, 207–220.

Kozlowski, C., and Weimer, R.M. (2012). An automated method to quantify microglia morphology and application to monitor activation state longitudinally in vivo. PLoS ONE *7*, e31814.

Krasemann, S., Madore, C., Cialic, R., Baufeld, C., Calcagno, N., El Fatimy, R., Beckers, L., O'Loughlin, E., Xu, Y., Fanek, Z., et al. (2017). The TREM2-APOE Pathway Drives the Transcriptional Phenotype of Dysfunctional Microglia in Neurodegenerative Diseases. Immunity *47*, 566–581.e9.

Lee, S., Lee, H.C., Kwon, Y.W., Lee, S.E., Cho, Y., Kim, J., Lee, S., Kim, J.Y., Lee, J., Yang, H.M., et al. (2014). Adenylyl cyclase-associated protein 1 is a receptor for human resistin and mediates inflammatory actions of human monocytes. Cell Metab. *19*, 484–497.

Li, H., and Durbin, R. (2009). Fast and accurate short read alignment with Burrows-Wheeler transform. Bioinformatics *25*, 1754–1760.

Li, Q., Cheng, Z., Zhou, L., Darmanis, S., Neff, N.F., Okamoto, J., Gulati, G., Bennett, M.L., Sun, L.O., Clarke, L.E., et al. (2019). Developmental Heterogeneity of Microglia and Brain Myeloid Cells Revealed by Deep Single-Cell RNA Sequencing. Neuron *101*, 207–223.e10.

Madry, C., Kyrargyri, V., Arancibia-Cárcamo, I.L., Jolivet, R., Kohsaka, S., Bryan, R.M., and Attwell, D. (2018). Microglial Ramification, Surveillance, and Interleukin-1β Release Are Regulated by the Two-Pore Domain K+Channel THIK-1. Neuron *97*, 299–312.e6.

Masuda, T., Sankowski, R., Staszewski, O., Böttcher, C., Amann, L., Scheiwe, C., Nessler, S., Kunz, P., van Loo, G., Coenen, V.A., et al. (2019). Spatial and temporal heterogeneity of mouse and human microglia at single-cell resolution. Nature *566*, 388–392.

Matcovitch-Natan, O., Winter, D.R., Giladi, A., Vargas Aguilar, S., Spinrad, A., Sarrazin, S., Ben-Yehuda, H., David, E., Zelada González, F., Perrin, P., et al. (2016). Microglia development follows a stepwise program to regulate brain homeostasis. Science *353*, aad8670.

Matesic, L.E., Yip, R., Reuss, A.E., Swing, D.A., O'Sullivan, T.N., Fletcher, C.F., Copeland, N.G., and Jenkins, N.A. (2001). Mutations in Mlph, encoding a member of the Rab effector family, cause the melanosome transport defects observed in leaden mice. Proc. Natl. Acad. Sci. USA *98*, 10238–10243.

Mathys, H., Adaikkan, C., Gao, F., Young, J.Z., Manet, E., Hemberg, M., De Jager, P.L., Ransohoff, R.M., Regev, A., and Tsai, L.H. (2017). Temporal Tracking of Microglia Activation in Neurodegeneration at Single-Cell Resolution. Cell Rep. *21*, 366–380.

McLean, C.Y., Bristor, D., Hiller, M., Clarke, S.L., Schaar, B.T., Lowe, C.B., Wenger, A.M., and Bejerano, G. (2010). GREAT improves functional interpretation of cis-regulatory regions. Nat. Biotechnol. *28*, 495–501.

Mellins, E.D., and Stern, L.J. (2014). HLA-DM and HLA-DO, key regulators of MHC-II processing and presentation. Curr. Opin. Immunol. *26*, 115–122.

Meyer-Luehmann, M., Spires-Jones, T.L., Prada, C., Garcia-Alloza, M., de Calignon, A., Rozkalne, A., Koenigsknecht-Talboo, J., Holtzman, D.M., Bacskai, B.J., and Hyman, B.T. (2008). Rapid appearance and local toxicity of amyloid-β plaques in a mouse model of Alzheimer's disease. Nature *451*, 720–724.

Mittal, K., Eremenko, E., Berner, O., Elyahu, Y., Strominger, I., Apelblat, D., Nemirovsky, A., Spiegel, I., and Monsonego, A. (2019). CD4 T cells Induce A Subset of MHCII-Expressing Microglia that Attenuates Alzheimer's Pathology. IScience *16*, 298–311.

Mosher, K.I., and Wyss-Coray, T. (2014). Microglial dysfunction in brain aging and Alzheimer's disease. Biochem. Pharmacol. *88*, 594–604.

Nishitsuji, K., Hosono, T., Uchimura, K., and Michikawa, M. (2011). Lipoprotein lipase is a novel amyloid β (Abeta)-binding protein that promotes glycosaminoglycan-dependent cellular uptake of Abeta in astrocytes. J. Biol. Chem. *286*, 6393–6401.

Ofengeim, D., Mazzitelli, S., Ito, Y., DeWitt, J.P., Mifflin, L., Zou, C., Das, S., Adiconis, X., Chen, H., Zhu, H., et al. (2017). RIPK1 mediates a disease-associated microglial response in Alzheimer's disease. Proc. Natl. Acad. Sci. USA *114*, E8788–E8797.

Parhizkar, S., Arzberger, T., Brendel, M., Kleinberger, G., Deussing, M., Focke, C., Nuscher, B., Xiong, M., Ghasemigharagoz, A., Katzmarski, N., et al. (2019). Loss of TREM2 function increases amyloid seeding but reduces plaque-associated ApoE. Nat. Neurosci. *22*, 191–204.

Perlmutter, L.S., Scott, S.A., Barrón, E., and Chui, H.C. (1992). MHC class II-positive microglia in human brain: Association with Alzheimer lesions. J. Neurosci. Res. *33*, 549–558.

Perry, V.H., and Holmes, C. (2014). Microglial priming in neurodegenerative disease. Nat. Rev. Neurol. *10*, 217–224.

Perry, V.H., and Teeling, J. (2013). Microglia and macrophages of the central nervous system: the contribution of microglia priming and systemic inflammation to chronic neurodegeneration. Semin. Immunopathol. *35*, 601–612.

Quinlan, A.R., and Hall, I.M. (2010). BEDTools: a flexible suite of utilities for comparing genomic features. Bioinformatics *26*, 841–842.

Ramírez, F., Ryan, D.P., Grüning, B., Bhardwaj, V., Kilpert, F., Richter, A.S., Heyne, S., Dündar, F., and Manke, T. (2016). deepTools2: a next generation web server for deep-sequencing data analysis. Nucleic Acids Res. *44*, W160–W165.

Ransohoff, R.M., and El Khoury, J. (2016). Microglia in health and disease. Cold Spring Harb. Perspect. Biol. *8*, a020560.

Ransohoff, R.M., and Perry, V.H. (2009). Microglial physiology: unique stimuli, specialized responses. Annu. Rev. Immunol. *27*, 119–145.

Robinson, J.T., Thorvaldsdóttir, H., Winckler, W., Guttman, M., Lander, E.S., Getz, G., and Mesirov, J.P. (2011). Integrative genomics viewer. Nat. Biotechnol. *29*, 24–26.

Roche, P.A., and Furuta, K. (2015). The ins and outs of MHC class II-mediated antigen processing and presentation. Nat. Rev. Immunol. *15*, 203–216.

Sala Frigerio, C., Wolfs, L., Fattorelli, N., Thrupp, N., Voytyuk, I., Schmidt, I., Mancuso, R., Chen, W.T., Woodbury, M.E., Srivastava, G., et al. (2019). The Major Risk Factors for Alzheimer's Disease: Age, Sex, and Genes Modulate the Microglia Response to Aβ Plaques. Cell Rep. *27*, 1293–1306.e6.

Schafer, D.P., and Stevens, B. (2015). Microglia function in central nervous system development and plasticity. Cold Spring Harb. Perspect. Biol. *7*, a020545.

Schmidl, C., Rendeiro, A.F., Sheffield, N.C., and Bock, C. (2015). ChIPmentation: fast, robust, low-input ChIP-seq for histones and transcription factors. Nat. Methods *12*, 963–965.

Schmitz, J., Owyang, A., Oldham, E., Song, Y., Murphy, E., McClanahan, T.K., Zurawski, G., Moshrefi, M., Qin, J., Li, X., et al. (2005). IL-33, an interleukin-1-like cytokine that signals via the IL-1 receptor-related protein ST2 and induces T helper type 2-associated cytokines. Immunity *23*, 479–490.

Sima, J., Yan, Z., Chen, Y., Lehrmann, E., Zhang, Y., Nagaraja, R., Wang, W., Wang, Z., and Schlessinger, D. (2018). Eda-activated RelB recruits an SWI/SNF (BAF) chromatin-remodeling complex and initiates gene transcription in skin appendage formation. Proc. Natl. Acad. Sci. USA *115*, 8173–8178.

Song, W.M., and Colonna, M. (2018). The identity and function of microglia in neurodegeneration. Nat. Immunol. *19*, 1048–1058.

Trost, M., English, L., Lemieux, S., Courcelles, M., Desjardins, M., and Thibault, P. (2009). The phagosomal proteome in interferon-γ-activated macrophages. Immunity *30*, 143–154.

Ulrich, J.D., Ulland, T.K., Mahan, T.E., Nyström, S., Nilsson, K.P., Song, W.M., Zhou, Y., Reinartz, M., Choi, S., Jiang, H., et al. (2018). ApoE facilitates the microglial response to amyloid plaque pathology. J. Exp. Med. *215*, 1047–1058.

van den Elsen, P.J. (2011). Expression regulation of major histocompatibility complex class I and class II encoding genes. Front. Immunol. *2*, 48.

Vom Berg, J., Prokop, S., Miller, K.R., Obst, J., Kälin, R.E., Lopategui-Cabezas, I., Wegner, A., Mair, F., Schipke, C.G., Peters, O., et al. (2012). Inhibition of IL-12/IL-23 signaling reduces Alzheimer's disease-like pathology and cognitive decline. Nat. Med. *18*, 1812–1819.

Wang, S., and Colonna, M. (2019). Microglia in Alzheimer's disease: A target for immunotherapy. J. Leukoc. Biol. *106*, 219–227.

Wang, Y., Cella, M., Mallinson, K., Ulrich, J.D., Young, K.L., Robinette, M.L., Gilfillan, S., Krishnan, G.M., Sudhakar, S., Zinselmeyer, B.H., et al. (2015). TREM2 lipid sensing sustains the microglial response in an Alzheimer's disease model. Cell *160*, 1061–1071.

Yeh, H., and Ikezu, T. (2019). Transcriptional and Epigenetic Regulation of Microglia in Health and Disease. Trends Mol. Med. *25*, 96–111.

Zhang, H., Ghai, P., Wu, H., Wang, C., Field, J., and Zhou, G.L. (2013). Mammalian adenylyl cyclase-associated protein 1 (CAP1) regulates cofilin function, the actin cytoskeleton, and cell adhesion. J. Biol. Chem. *288*, 20966–20977.

Zhang, X., Tian, Y., Zhang, C., Tian, X., Ross, A.W., Moir, R.D., Sun, H., Tanzi, R.E., Moore, A., and Ran, C. (2015). Near-infrared fluorescence molecular

imaging of amyloid beta species and monitoring therapy in animal models of Alzheimer's disease. Proc. Natl. Acad. Sci. USA *112*, 9734–9739.

Zhao, J., Wei, J., Mialki, R.K., Mallampalli, D.F., Chen, B.B., Coon, T., Zou, C., Mallampalli, R.K., and Zhao, Y. (2012). F-box protein FBXL19-mediated ubiquitination and degradation of the receptor for IL-33 limits pulmonary inflammation. Nat. Immunol. *13*, 651–658.

Zheng, G.X.Y., Terry, J.M., Belgrader, P., Ryvkin, P., Bent, Z.W., Wilson, R., Ziraldo, S.B., Wheeler, T.D., McDermott, G.P., Zhu, J., et al. (2017). Massively parallel digital transcriptional profiling of single cells. Nat. Commun. *8*, 14049.

STAR★METHODS

KEY RESOURCES TABLE

REAGENT or RESOURCE	SOURCE	IDENTIFIER
Antibodies		
Rabbit anti-Iba1	Wako	Cat # 019-19741
Rat anti-CD11b (M1/70.15) Pacific Blue	Life Technologies	Cat # RM2828
Rat anti-CD11b (M1/70) Alexa Fluor 488	eBioscience	Cat # 53-0112-82
Rat anti-CD45 (clone 30-F11) FITC	eBioscience	Cat # 11-0451-85
Rat anti-CD68 (clone FA-11) PE	eBioscience	Cat # 12-0681-82
Rat anti-MHC Class II (I-A/I-E; clone M5/114.15.2) PE-Cyanine5	eBioscience	Cat # 15-5321-81
Rabbit anti-PU.1	Cell Signaling Technology	Cat # 2258
Rabbit anti-H3K4me3 antibody	Active Motif	Cat # 39159
Mouse anti-Aβ (clone 6E10) Alexa Fluor 488	Biolegend	Cat # 803013
Mouse anti-Aβ (clone 6E10) Alexa Fluor 647	Biolegend	Cat # 803021
Rat anti-MHC class II I-A/I-E (clone M5/114.15.2)	Biolegend	Cat # 107601
Chemicals, Peptides, and Recombinant Proteins		
Murine recombinant IL-33	Biolegend	Cat # 580506
CRANAD-3	Gift by Dr. Chongzhao Ran's laboratory (Zhang et al., 2015)	NA
DNase I	Worthington Biochemical	Cat # LS002140
Papain	Worthington Biochemical	Cat # LS003126
Methoxy-X04	Tocris Bioscience	Cat # 4920
Mouse FcR blocking reagent	Miltenyi Biotec	Cat # 130-092-575
DB2313	Glixx Laboratories	Cat # GLXC-11111
Critical Commercial Assays		
RNAscope Multiplex Fluorescent Reagent Kit v2	ACD Bioscience	Cat # 323100
Chromium Single Cell 3′ Library Kit v2	10x Genomics	Cat # 120237
Nextera DNA Library Preparation Kit	Illumina	Cat # FC-121-1030
Deposited Data		
Raw and analyzed data	This paper	GEO: GSE147495
Experimental Models: Cell Lines		
BV2	Gift by Dr. Douglas Golenbock's laboratory	NA
Experimental Models: Organisms/Strains		
Mouse: APP/PS1	The Jackson Laboratory	Cat # 34829-JAX
Mouse: Cx3cr1$^{eYFP/+}$	The Jackson Laboratory	Cat # 021160
Oligonucleotides		
PU.1 anti-sense oligonucleotides: 5′-TTTGCACG CCTGTAACATCCAGCTGACCTC-3′ (Celada et al., 1996)	Life Technologies	NA
Software and Algorithms		
Imaris	Bitplane	https://imaris.oxinst.com
FlowJo	TreeStar	https://www.flowjo.com
Cell Ranger (version 3.0)	10x Genomics	Zheng et al., 2017
Seurat (version 3.0)	Butler et al., 2018	https://satijalab.org/seurat/
STRING	https://string-db.org/	NA

(*Continued on next page*)

Continued

REAGENT or RESOURCE	SOURCE	IDENTIFIER
Morpheus	https://software.broadinstitute.org/morpheus	NA
Burrows–Wheeler Aligner	Li and Durbin, 2009	http://bio-bwa.sourceforge.net
Picard tools	http://broadinstitute.github.io/picard	NA
HOMER	Heinz et al., 2010	http://homer.ucsd.edu/homer/
bedtools	Quinlan and Hall, 2010	https://bedtools.readthedocs.io/en/latest/
deepTools	Ramírez et al., 2016	https://deeptools.readthedocs.io/en/develop/

RESOURCE AVAILABILITY

Lead Contact

Further information and requests for resources and reagents should be directed to and will be fulfilled by the Lead Contact, Nancy Yuk-Yu Ip (boip@ust.hk).

Materials Availability

This study did not generate new unique reagents.

Data and Code Availability

The accession number for the single-cell RNA-sequencing, ATAC-sequencing, anti-PU1, and anti-H3K4me3 ChIP-sequencing datasets reported in this paper is GEO repository: GSE147495.

EXPERIMENTAL MODEL AND SUBJECT DETAILS

All mice were housed at the Hong Kong University of Science and Technology (HKUST) Animal and Plant Care Facility, and all animal experiments were performed in accordance with protocols #2017046 and #2017048, which were approved by the Animal Care Committee of HKUST. Mice of the same sex were housed four per cage with a 12-h light/dark cycle, and food and water *ad libitum*. All experiments were performed on sex- and age-matched (10–12 months old) groups. Mice of both genders were used for experiments. The mice were randomized to the experimental conditions. Sample sizes were chosen primarily on the basis of experience with similar types of experiments.

APP/PS1 transgenic mice, which were generated by incorporating a human/murine APP construct bearing the Swedish double mutation and the exon-9–deleted PSEN1 mutation (APPswe + PSEN1/dE9), were obtained from the Jackson Laboratory (B6C3-Tg[APPswe, PSEN1dE9]85Dbo). Cx3cr1^{eYFP} mice, in which eYFP expression is controlled by a microglia-specific promoter, were also obtained from the Jackson Laboratory (B6.129P2[Cg]-Cx3cr1$^{tm2.1[cre/ERT2]Litt}$). Genotypes were confirmed by PCR analysis of ear biopsy specimens.

METHOD DETAILS

Reagents

Murine recombinant IL-33 (580506) was obtained from Biolegend. CRANAD-3 was kindly provided by Chongzhao Ran's laboratory at Massachusetts General Hospital and Harvard Medical School. DNase I (LS002140) and Papain (LS003126) were obtained from Worthington Biochemical. Iba1 antibody (019-19741) was obtained from Wako. Pacific blue-conjugated CD11b (clone M1/70.15; RM2828) antibody was obtained from Life Technologies. Alexa Fluor 488-conjugated CD11b antibody (clone M1/70; 53-0112-82) antibody, FITC-conjugated CD45 antibody (clone 30-F11; 11-0451-85), PE-conjugated CD68 antibody (clone FA-11; 12-0681-82), and PE-Cyanine5-conjugated MHC Class II antibody (I-A/I-E; clone M5/114.15.2; 15-5321-81) were obtained from eBioscience. PU.1 antibody (2258) was obtained from Cell Signaling Technology. H3K4me3 antibody (39159) was obtained from Active Motif. Alexa Fluor 488-conjugated monoclonal Aβ antibody (clone 6E10; 803013), Alexa Fluor 647-conjugated monoclonal Aβ antibody (clone 6E10; 803021), and MHC class II I-A/I-E antibody (clone M5/114.15.2; 107601) were obtained from Biolegend. Methoxy-X04 (MeX04; 4920) was obtained from Tocris Bioscience. Mouse FcR blocking reagent (130-092-575) was obtained from Miltenyi Biotec. DB2313 (GLXC-11111) was obtained Glixx Laboratories.

In vivo experiments

Mice (10–12 months old) were intraperitoneally injected with 200 ng murine recombinant IL-33 for 2 consecutive days and sacrificed on day 3, except for *in vivo* imaging experiments and experiments involving PU.1 inhibition; for *in vivo* imaging experiments, a single

injection of IL-33 was administered during the imaging session. To analyze Aβ phagocytosis by microglia *in vivo*, the mice were intraperitoneally injected with MeX04 10 mg/kg 3 h before sacrifice on day 3. For PU.1 inhibition studies, 10 mM DB2313 stock solution was prepared by dissolving DB2313 in DMSO; 170 μM working DB2313 solution was prepared by diluting the stock solution in artificial cerebrospinal fluid (119 mM NaCl, 2.5 mM KCl, 2.5 mM $CaCl_2 \cdot 2H_2O$, 1 mM $NaH_2PO_4 \cdot 2H_2O$, 1.3 mM $MgCl_2 \cdot 6H_2O$, 26.2 mM $NaHCO_3$, and 11 mM D-glucose). DMSO (same volume as the stock solution) diluted in artificial cerebrospinal fluid was used as vehicle control (Veh). APP/PS1 mice were intracerebroventricularly injected with 2.5 μL 170 μM working DB2313 solution or Veh at 0.2 μL/min at the following coordinates relative to the bregma: anteroposterior, −0.3 mm, mediolateral; +1.2 mm; and dorsoventral: −2.3 mm. IL-33 was injected intraperitoneally 24 h later, and mice were sacrificed 15 h later.

In vivo two-photon imaging of microglia

In vivo imaging was performed with a home-built two-photon microscopy system as previously described (Chen et al., 2018). In brief, 10- to 12-month-old APP/PS1;$Cx3cr1^{eYFP/+}$ mice were used. Mice were anesthetized with isoflurane and subsequently underwent thin-skull surgery 24 h before imaging. A small region 1.0 mm in diameter centered at 2 mm lateral and 3 mm posterior to the bregma was thinned down to 40–50 μm thickness. A plastic head plate was placed over the center of the region to be mounted on the skull for head fixation during *in vivo* imaging. Postoperatively, the mice were transferred to a 37°C heating plate and returned to their home cages after fully recovering. CRANAD-3 (an infrared-red Aβ dye) (Zhang et al., 2015) was injected into the tail vein at 2 mg/kg 3 h before IL-33 (200 ng) injection. Images were acquired 0.5 h before and every 1.5 h after injection for 12 h. The animals were under isoflurane (0.5%–1.5%) anesthesia during all imaging sessions, with a heating pad set at 37°C to maintain body temperature. The laser was tuned to 960 nm to excite both eYFP and CRANAD-3, and the optical power was kept below 80 mW to prevent photo-damage to the brain tissue. Two fluorescent channels—525 ± 25 and 650 ± 30 nm—separated by a dichroic mirror (T560lpxr, Chroma) were used to collect the fluorescence signals of eYFP and CRANAD-3, respectively. After the imaging experiment, the mice were allowed to recover from anesthesia and returned to their home cages.

For data analysis, the migration distance of microglia and their relative distance to Aβ plaques were determined by Imaris (Bitplane). For Figure 1F, some high-mobility microglia were excluded from analysis because of the ambiguity of which Aβ plaque was nearest. The ramification index of microglia was determined using ImageJ and MATLAB scripts as previously described (Madry et al., 2018).

In situ hybridization by RNAscope

Adult mice were deeply anesthetized using isoflurane, and their brains were isolated and frozen immediately on dry ice. Fresh frozen sections (16 μm) were prepared using a cryostat. *In situ* hybridization was performed using an RNAscope Multiplex Fluorescent Reagent Kit v2 (323100) according to the manufacturer's instructions. The RNAscope probes targeting *Cx3cr1*, *Cst7*, *Fcrls*, and *H2-Ab1* were purchased from Advanced Cell Diagnostics. Microglial subpopulation proportions and RNA puncta were quantified manually using ImageJ. We considered a cell to be positively expressing our target genes when they had at least four puncta for the corresponding gene.

Flow cytometry and fluorescence-activated cell sorting

Adult mice were deeply anesthetized using isoflurane and perfused with ice-cold DPBS. The forebrain was isolated, minced into small pieces, dissociated enzymatically in papain (5 U/mL) and DNase I (50 U/mL) for 30 min at 37°C, and then triturated gently. A Percoll gradient (30%; Sigma-Aldrich) was used to remove myelin. The resultant mononuclear cell suspensions were used for cell sorting in a BD Influx cell sorter or flow cytometry analysis in a BD FACSAria III. Unstained controls were used to identify cell populations. Clear subpopulations of microglia were visualized on scatterplots, and the purity of microglial isolation was routinely >90% according to re-analysis of the sorted cells. Data were analyzed using FlowJo software (TreeStar).

scRNA-seq library preparation

scRNA-seq libraries were generated using the Chromium Single Cell 3′ Library Kit v2 (120237; 10x Genomics) according to the manufacturer's instructions. In brief, sorted myeloid cells were washed once and counted on a hemocytometer. Single-cell suspensions (300–1,000 cells/μL) were mixed with reverse-transcription reagent mix and loaded into the chip for single-cell encapsulation. Encapsulated cells were immediately incubated on a thermocycler for reverse transcription. Barcoded cDNA was obtained and used for library construction according to the manufacturer's instructions. The concentrations of the final libraries were quantified by Qubit (Thermo Fisher), and fragment lengths were quantified by Fragment Analyzer (Advanced Analytical). Libraries were paired-end sequenced on a NextSeq 500 according to the manufacturer's instructions.

scRNA-seq analysis

The sequencing data were aligned, quantified, and clustered using Cell Ranger (version 3.0) as previously described (Zheng et al., 2017). Seurat (version 3.0) (Butler et al., 2018) was used for the initial quality control for *t*-SNE clustering. Re-clustering was performed using the Cell Ranger pipeline. Next, *t*-SNE plots were generated, and the DEGs (adjusted p value <0.1, $\log_2$ fold change >0.56 or <−0.56) were identified using *Seurat* (version 3.0). Cell type identification analysis showed that ~95% of the $CD11b^+$ cells were

myeloid cells (Figure S2G). Gene expression at the single-cell level was determined using cellrangerRkit and visualized with Morpheus and Seurat *DotPlot* function. DEGs were functionally annotated by GO and STRING.

Immunohistochemistry

Adult mice were deeply anesthetized using isoflurane and perfused with ice-cold DPBS. Their brains were isolated and fixed overnight in 4% PFA. Then, 50-μm floating sections were prepared using a vibratome.

To study the induction of IL-33RM, their localization with Aβ plaques and lysosomal activities were examined. Aβ was labeled *in vivo* with MeX04 (2 mg/kg) 3 h before sacrifice. Floating sections (50 μm) were blocked with 1% BSA, 4% horse serum, and 0.4% Triton X-100 in Dulbecco's PBS (DPBS) at room temperature for 30 min and then incubated with PE-conjugated CD68 (1:1,000 dilution), Iba1 (1:500 dilution), and MHC-II (1:300 dilution) overnight at 4°C. After washing, sections were incubated with respective secondary antibodies (all at 1:1,000 dilution) at room temperature for 2 h. Confocal images were acquired using a Leica TCS SP8 confocal microscope or a Zeiss LSM880 confocal microscope. ImageJ and LAS X (Leica) were used to quantify cells and CD68/Iba1 area.

To study the Aβ plaque load in APP/PS1 mice, 6E10 immunostaining was performed. First, antigen retrieval was performed by incubating sections in sodium citrate buffer (10 mM trisodium citrate and 0.5% Tween-20 in H_2O [pH 6.0]) at 80°C for 10 min. The sections were blocked with 1% BSA, 4% horse serum, and 0.4% Triton X-100 in DPBS at room temperature for 30 min, followed by incubation with Alexa Fluor 488-conjugated monoclonal 6E10 antibody (1:1,000 dilution) overnight at 4°C.

Imaging was performed using a Leica DM6000 B compound microscope system. Representative images were taken using Zeiss LSM880 confocal microscope. The area of Aβ plaques in the cortex in the brain coronal sections was analyzed using the *Analyze Particles* function of ImageJ. Three brain sections per mouse (~200–300 μm apart near the hippocampus) were analyzed, and the average percentage of the cortical area occupied by Aβ plaques was calculated.

ATAC-seq library preparation

ATAC-seq libraries were generated as previously described with minor modifications (Buenrostro et al., 2013). In brief, approximately 50,000 sorted cells were washed once with ice-cold DPBS. Nuclei were extracted using 50 μL ice-cold lysis buffer (10 mM Tris·Cl [pH 7.4], 10 mM NaCl, 3 mM $MgCl_2$, and 0.1% [v/v] Igepal CA-630). The extracted nuclei were tagmented by incubation with Tn5 transposase (Illumina) for 30 min at 37°C. Tagmented genomic DNA was then amplified by PCR for 15 cycles. The libraries were size-selected (100–600 bp) by Ampure XP beads (Beckman Coulter). The concentrations of the final libraries were quantified by Qubit (Thermo Fisher), and fragment lengths were quantified by Fragment Analyzer (Advanced Analytical). The pooled libraries were paired-end sequenced on a NextSeq 500.

ChIP-seq library preparation

The cells were fixed immediately after staining and then subjected to sorting. The cell pellets were fixed with 1% PFA at room temperature for 10 min and quenched with 0.125 M glycine at room temperature for 5 min. The fixed cells were washed once, and microglia were sorted as described above. Sorted microglia were then snap-frozen in liquid nitrogen and stored at −80°C until use. ChIP-seq libraries were constructed using ChIPmentation, which is an optimized method for low-input ChIP-seq library preparation (Schmidl et al., 2015). In brief, approximately 200,000–300,000 sorted cells were resuspended in 0.25% SDS sonication buffer with protease inhibitors. Genomic DNA was sonicated into 200–700-bp fragments using a Covaris S220 focused-ultrasonicator system (Covaris). Fragmented genomic DNA was diluted 1:1.5 in equilibration buffer (10 mM Tris, 233 mM NaCl, 1.66% Triton X-100, 0.166% sodium-deoxycholate [Na-DOC], 1 mM EDTA, and protease inhibitors) and incubated with antibodies targeting PU.1 (3 μL) or H3K4me3 (2 μg) overnight at 4°C. Protein A Dynabeads (Thermo Fisher) were washed twice and incubated with 0.1% BSA/RIPA overnight at 4°C. After overnight blocking, 10 μL pre-blocked beads was added to each sample and incubated at 4°C for 2 h. Protein-bound beads were then washed twice with ice-cold RIPA-LS buffers (10 mM Tris-HCl [pH 8.0], 140 mM NaCl, 1 mM EDTA [pH 8.0], 0.1% SDS, 0.1% Na-DOC, and 1% Triton X-100), twice with ice-cold RIPA-HS buffer (10 mM Tris-HCl [pH 8.0], 500 mM NaCl, 1 mM EDTA [pH 8.0], 0.1% SDS, 0.1% Na-DOC, and 1% Triton X-100), twice with ice-cold RIPA-LiCl buffer (10 mM Tris-HCl [pH 8.0], 250 mM LiCl, 1 mM EDTA [pH 8.0], 0.5% NP-40, and 0.5% Na-DOC), and twice with ice-cold 10 mM Tris (pH 8.0) buffer on a pre-cooled magnetic stand. ChIP products were tagmented on beads with Tn5 transposase (Illumina) at 37°C for 5 min. Tagmented ChIP products were washed once with ice-cold RIPA-LS buffer and once with ice-cold TE buffer (10 mM Tris-HCl [pH 8.0] and 1 mM EDTA [pH 8.0]). After washing, tagmented ChIP products were reverse-crosslinked with proteinase K (NEB) in ChIP elution buffer for 1 h at 55°C and then for 6 h at 65°C. DNA was purified using a QIAGEN MinElute Kit (28004). Purified DNA was subsequently amplified by PCR for 17–20 cycles, and the final libraries were size-selected (100–600 bp) by Ampure XP beads (Beckman Coulter). The concentrations of the final libraries were quantified by Qubit (Thermo Fisher), and fragment lengths were quantified by Fragment Analyzer (Advanced Analytical). Pooled libraries were single-end sequenced on a NextSeq 500.

ATAC-seq and ChIP-seq analyses

For sequencing alignment and duplicate removal, sequencing data were mapped to the mm10 mice genome assembly by using the Burrows–Wheeler Aligner's *bwa-mem* function (Li and Durbin, 2009). Duplicates were marked and removed using the Picard tools *MarkDuplicates* function with the parameter, *REMOVE_DUPLICATES = TRUE*. For peak identification, the HOMER (Heinz et al., 2010) *maketagdirectory* function was used to combine sequencing data from the biological replicates, and the *findPeaks* function

was used to identify binding/accessible regions with the following parameters: *-style factor* (for PU.1 ChIP-seq), *-style histone* (for H3K4me3 ChIP-seq), and *-style histone -minDist 200* (for ATAC-seq). Regions were annotated by the *annotatePeaks.pl* function. Read count in the binding/accessible regions was quantified by the bedtools (Quinlan and Hall, 2010) *multicov* function. Differential binding/accessible regions ($p < 0.05$) were calculated using an R script developed in house. The HOMER *mergePeaks* function was used to search for overlapping regions, which were visualized using Venn diagrams. To search for the enriched motifs in the targeted regions over the genome, the HOMER *findMotifsGenome.pl* function was used for the *de novo* motif search. To visualize mapped reads, bigWig files were generated using the deepTools (Ramírez et al., 2016) *bamCoverage* function and visualized in igv browser (Robinson et al., 2011).

PU.1 knockdown in BV2 cells by antisense oligonucleotides

BV2 cells were expanded in DMEM supplemented with 10% FBS, penicillin/streptomycin, and GlutaMAX (Thermo Fisher Scientific) and maintained in a humidified incubator containing 5% CO_2 at 37 °C. Cells were pre-treated with 300 nM of antisense oligonucleotides (5′-TTTGCACGCCTGTAACATCCAGCTGACCTC-3′) (Celada et al., 1996) targeting translation start site of PU.1 mRNA transcript for 24 h, and followed by 30 ng/mL IL-33 treatment for 12 h. Sense oligonucleotides were treated as control.

For qRT-PCR, RNA was extracted using Nucleospin Kit (Macherey Nagel) and quantified using a BioDrop μLITE microvolume spectrophotometer. Equivalent amounts of RNA were reverse-transcribed using the PrimeScript RT-PCR Kit (TaKaRa). The PCR amplification and real-time detection of PCR products were performed using TaqMan gene expression assay (Applied Biosystems) and Premix Ex Taq qPCR assay (TaKaRa). The copy numbers for samples were averaged across duplicates. The mRNA expression values were normalized to the level of β-actin. The following TaqMan probes were used: *H2-Ab1* (Mm00439216_m1) and *Actb* (Mm02619580_g1).

QUANTIFICATION AND STATISTICAL ANALYSIS

For scRNA-seq, differential analysis was calculated by Seurat *FindMarker* function and the threshold for calling statistical significance was adjusted p value < 0.1. For ATAC-seq and ChIP-seq, differential analysis was calculated by Student's t test in R and the threshold for calling statistical significance was p value < 0.05. The rest of the statistical analyses were performed using Graphpad PRISM 8.0. All the statistical details were described in the figure legends.

Cell Reports, Volume *31*

Supplemental Information

IL-33-PU.1 Transcriptome Reprogramming Drives Functional State Transition and Clearance Activity of Microglia in Alzheimer's Disease

Shun-Fat Lau, Congping Chen, Wing-Yu Fu, Jianan Y. Qu, Tom H. Cheung, Amy K.Y. Fu, and Nancy Y. Ip

Supplemental information

Figure S1. Related to Figure 1.

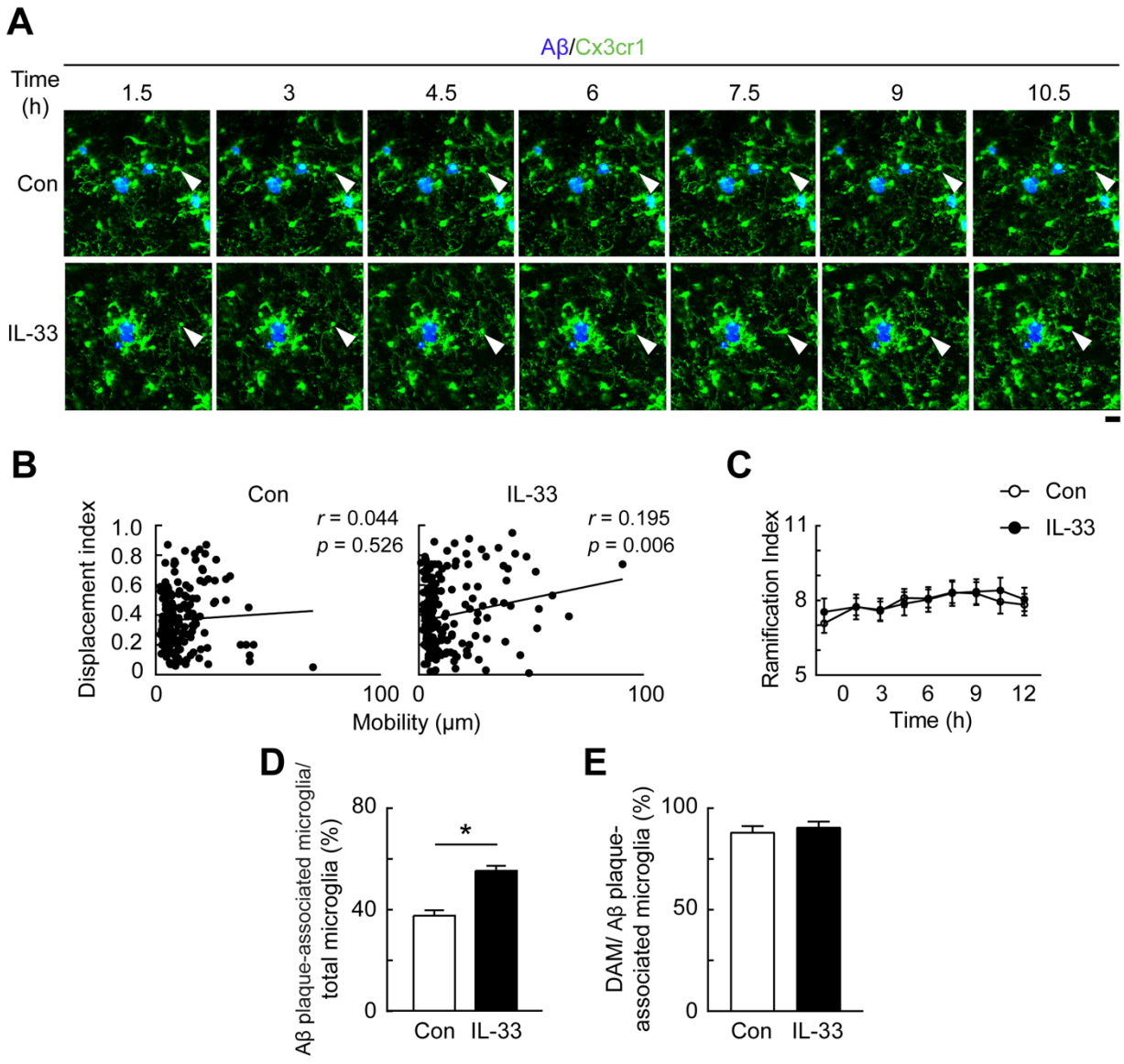

Figure S1. Interleukin-33 injection enhances the interaction of a microglial subpopulation with beta-amyloid plaques in APP/PS1 mice.

(A) Representative images showing the morphology of eYFP$^+$ microglia and their interaction with CRANAD-3$^+$ beta-amyloid (Aβ) plaques at each imaging timepoint after interleukin (IL)-33 injection. Arrowheads denote the same microglia. Scale bar = 20 μm. (B) Displacement index was positively correlated with microglial mobility upon IL-33 injection (DPBS-injected (Con): *n* = 110 microglia from three mice, IL-33: *n* = 274 microglia from four mice; linear regression). (C) Quantification of microglial ramification index at different timepoints in APP/PS1 mice with or without IL-33 injection (Con: *n* = 32 microglia from three mice, IL-33: *n* = 33 microglia from three mice). (D, E) IL-33 injection increased disease-associated microglia (DAM) interaction with 6E10$^+$ Aβ plaques. (D) Proportions of Aβ plaque-associated microglia (i.e., *Cx3cr1*$^+$ cells) in IL-33–injected and Con APP/PS1 mice (Con: *n* = 4, IL-33: *n* = 4; **p* < 0.05 vs. Con, Student's *t*-test). (E) Proportion of DAM (i.e., *Cst7*$^+$ *Cx3cr1*$^+$ cells) among Aβ plaque-associated microglia in IL-33–injected and Con APP/PS1 mice (Con: *n* = 4, IL-33: *n* = 4). All data are represented as mean ± SEM.

Figure S2. Related to Figure 2.

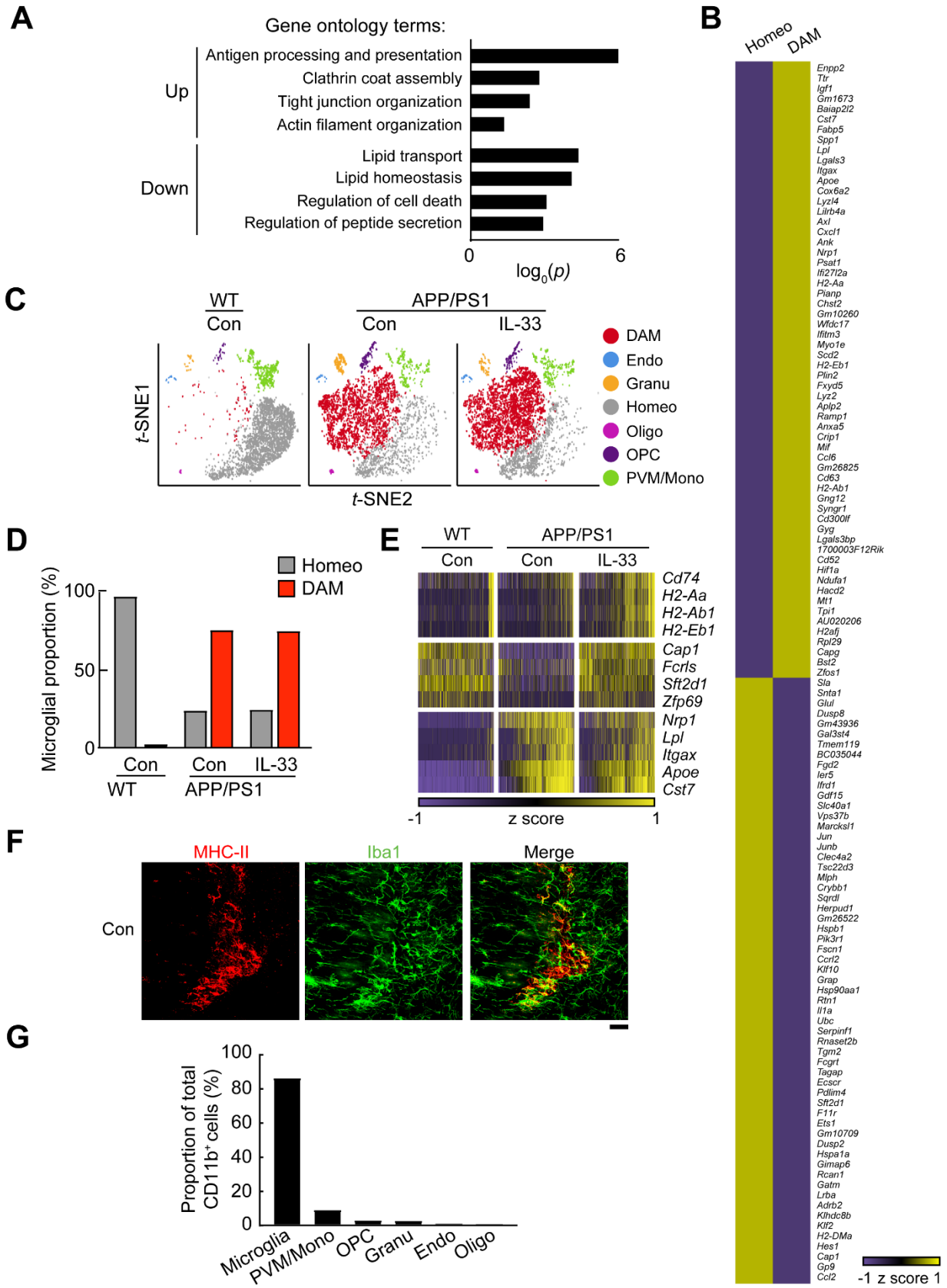

Figure S2. IL-33 reverses the microglial transcriptomic responses to Aβ.

(A) Pathway analysis of differentially expressed genes (DEGs) induced by IL-33 injection in microglia in APP/PS1 mice. (B) Heatmap showing the top 70 enriched genes in DAM and homeostatic microglia. (C, D) IL-33 injection did not regulate the proportion of DAM in APP/PS1 mice. (C) *t*-distributed stochastic neighbor embedding (*t*-SNE) plots showing the seven identified cell clusters in IL-33–injected APP/PS1 mice, Con APP/PS1 mice, and Con WT mice. (D) Proportions of DAM among the total microglia in each condition. (E) Heatmap showing the expression of MHC-II genes (i.e., *Cd74*, *H2-Ab1*, and *H2-Eb1*), homeostatic signature genes (i.e., *Cap1*, *Fcrls*, *Sft2d1*, and *Zfp69*), and DAM signature genes (i.e., *Apoe*, *Cst7*, *Itgax*, *Lpl*, and *Nrp1*) in microglia in each condition. (F) Representative images showing MHC-II$^+$ myeloid cells near choroid plexus in Con APP/PS1 mice. Scale bar = 40 μm. (G) Bar plot showing the proportion of different cell types in the scRNA-seq analysis.

Figure S3. Related to Figure 3.

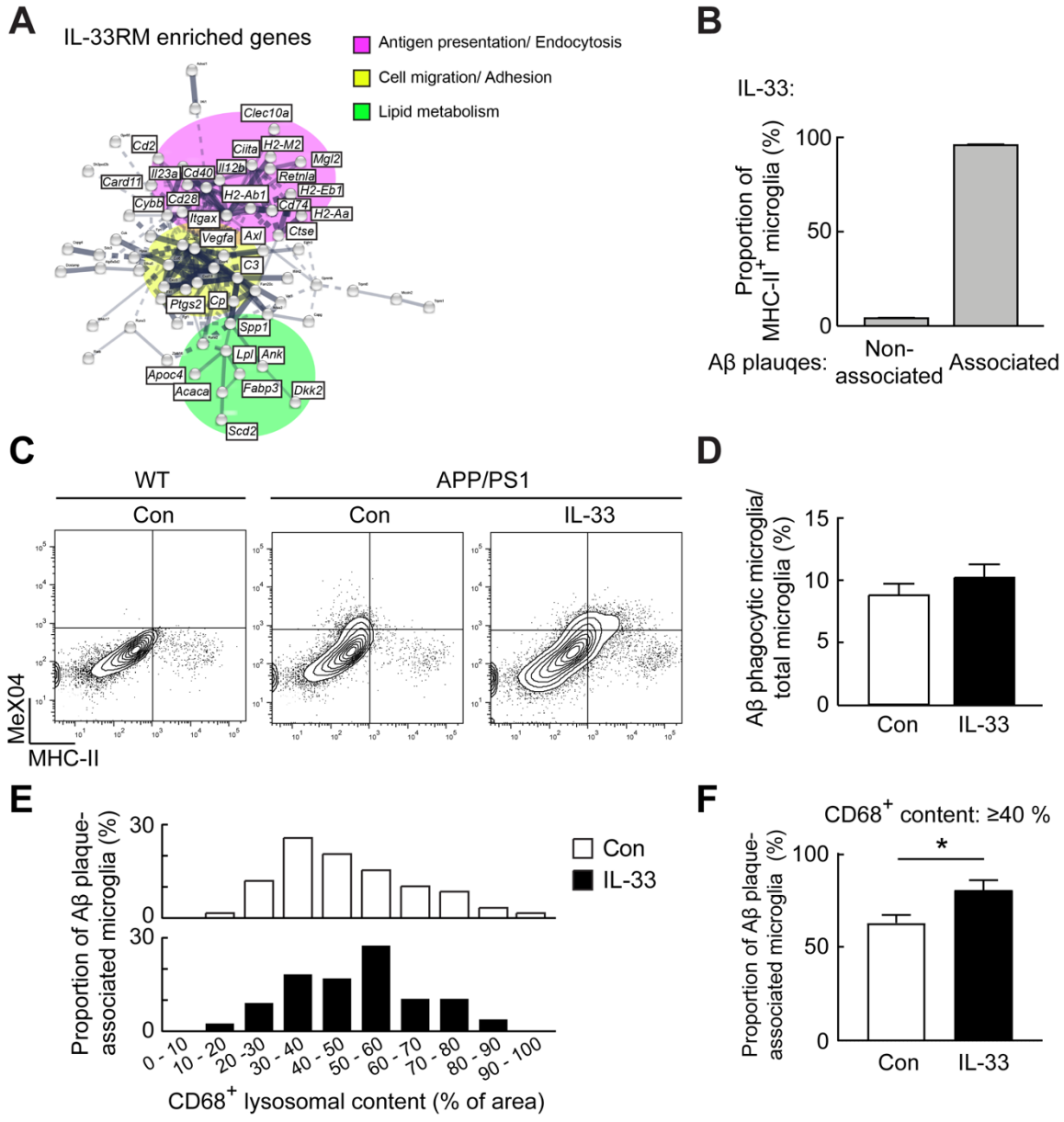

Figure S3. Functional characterization of IL-33RM in IL-33–injected APP/PS1 mice.

(A) STRING analysis of IL-33RM signature genes identified pathways associated with endocytosis and chemotaxis. Network analysis of IL-33RM-enriched genes. (B) Proportion of IL-33RM that associated with Aβ plaques in the cortices from IL-33–injected APP/PS1 mice (IL-33: $n = 4$). (C) Representative contour plots showing the MeX04 signal in IL-33–injected and Con APP/PS1 mice. WT mice was included as a baseline reference. (D) The proportions of Aβ-phagocytic microglia. Bar plot showing the proportions of Aβ-phagocytic microglia (i.e., MeX04$^+$ CD11b$^+$ cells) in the forebrain from IL-33–injected and Con APP/PS1 mice (Con: $n = 4$, IL-33: $n = 7$). (E, F) IL-33 increased the proportion of Aβ plaque-associated microglia with high CD68$^+$ lysosomal content in APP/PS1 mice. (E) Proportion of Aβ plaque-associated microglia binarized by CD68$^+$ lysosomal content (Con: $n = 50$ microglia from 6 mice; $n = 76$ microglia from 8 mice). (F) Proportion of Aβ plaque-associated microglia with high (≥40%) CD68$^+$ lysosomal content after IL-33 injection in APP/PS1 mice (Con: $n = 6$, IL-33: $n = 8$; $^*p < 0.05$ vs. Con, Student's *t*-test). All data are represented as mean ± SEM.

Figure S4. Related to Figure 4.

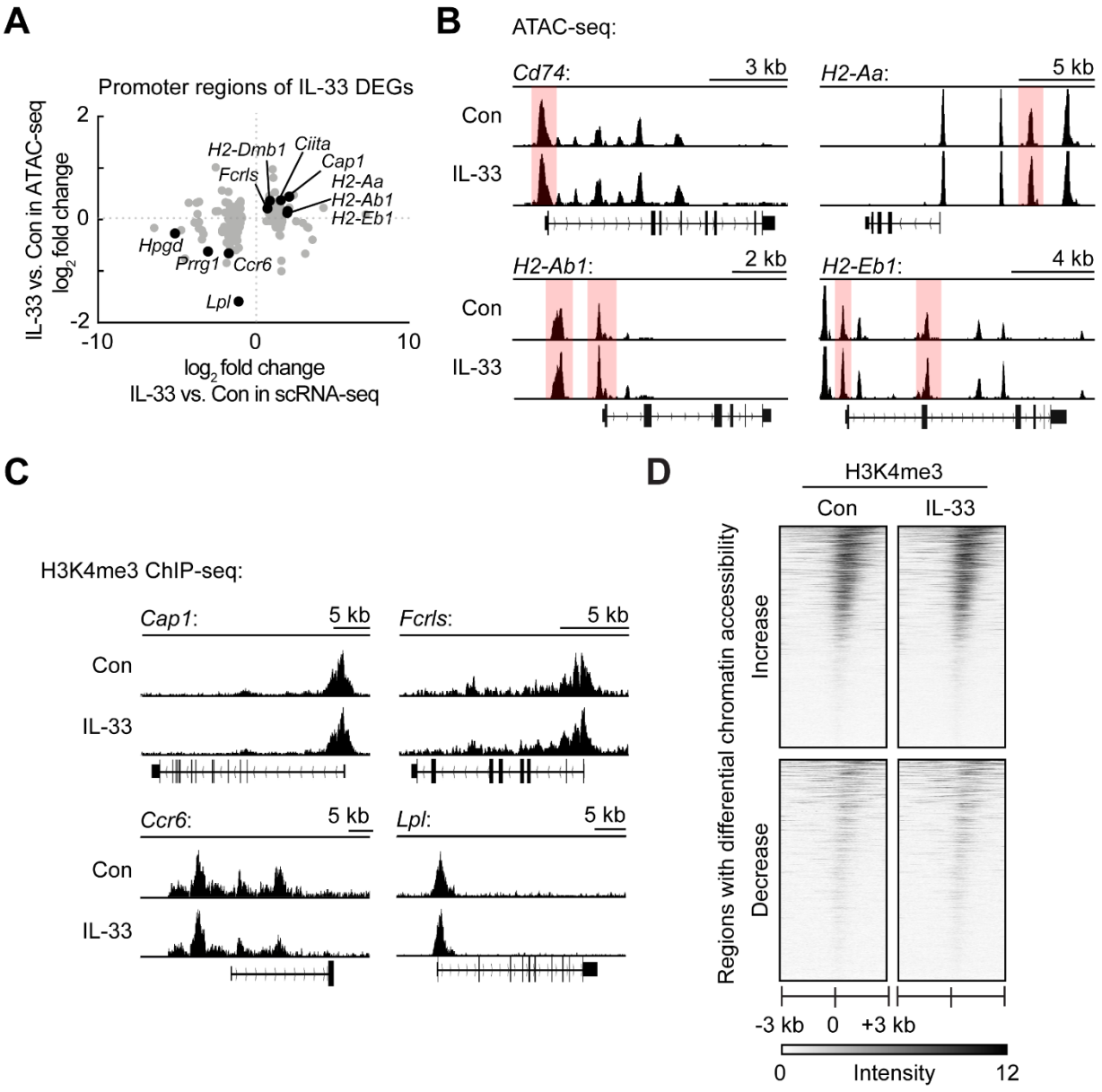

Figure S4. IL-33 regulates chromatin accessibility at the active promoters of IL-33 DEGs in APP/PS1 microglia.

(A–B) IL-33 injection regulated the chromatin accessibility of DEGs in microglia, which was positively correlated with their gene expression changes. (A) IL-33 injection increased chromatin accessibility at the regulatory regions of IL-33RM signature genes in microglia in APP/PS1 mice. Correlations between the changes in ATAC-seq signal intensity at the promoter regions of IL-33 DEGs and their gene expression changes upon IL-33 injection. (B) Visualization of the chromatin accessibility landscape at the regulatory regions of MHC-II genes in IL-33-treated and Con APP/PS1 mice. (C, D) Regions in which chromatin accessibility was modulated by IL-33 were enriched with H3K4me3, which indicates active promoter regions. (C) Visualization of the H3K4me3 landscape at the promoter regions of IL-33–upregulated genes (i.e., *Cap1* and *Fcrls*) and IL-33–downregulated genes (i.e., *Ccr6* and *Lpl*). (D) Heatmap showing H3K4me3 signals at regions ±3 kb from sites with differential chromatin accessibility upon IL-33 injection in APP/PS1 mice. All data are represented as mean ± SEM.

Figure S5. Related to Figure 5.

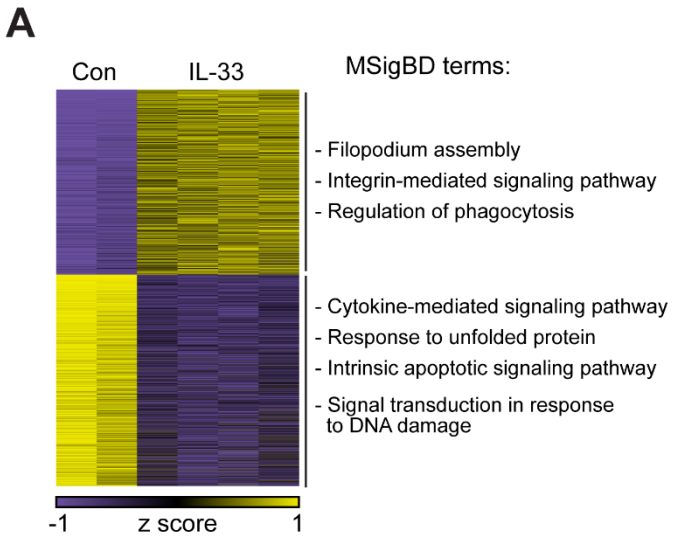

Figure S5. IL-33 injection regulates the PU.1-binding landscape in microglia in APP/PS1 mice.

(A) Heatmap showing the regions with differential PU.1 binding in APP/PS1 microglia upon IL-33 injection ($p < 0.05$; $\log_2$ fold change >0.263 or <−0.263). Highlighted MSigDB terms from GREAT analysis of the differential binding regions are listed.

Figure S6. Related to Figure 6.

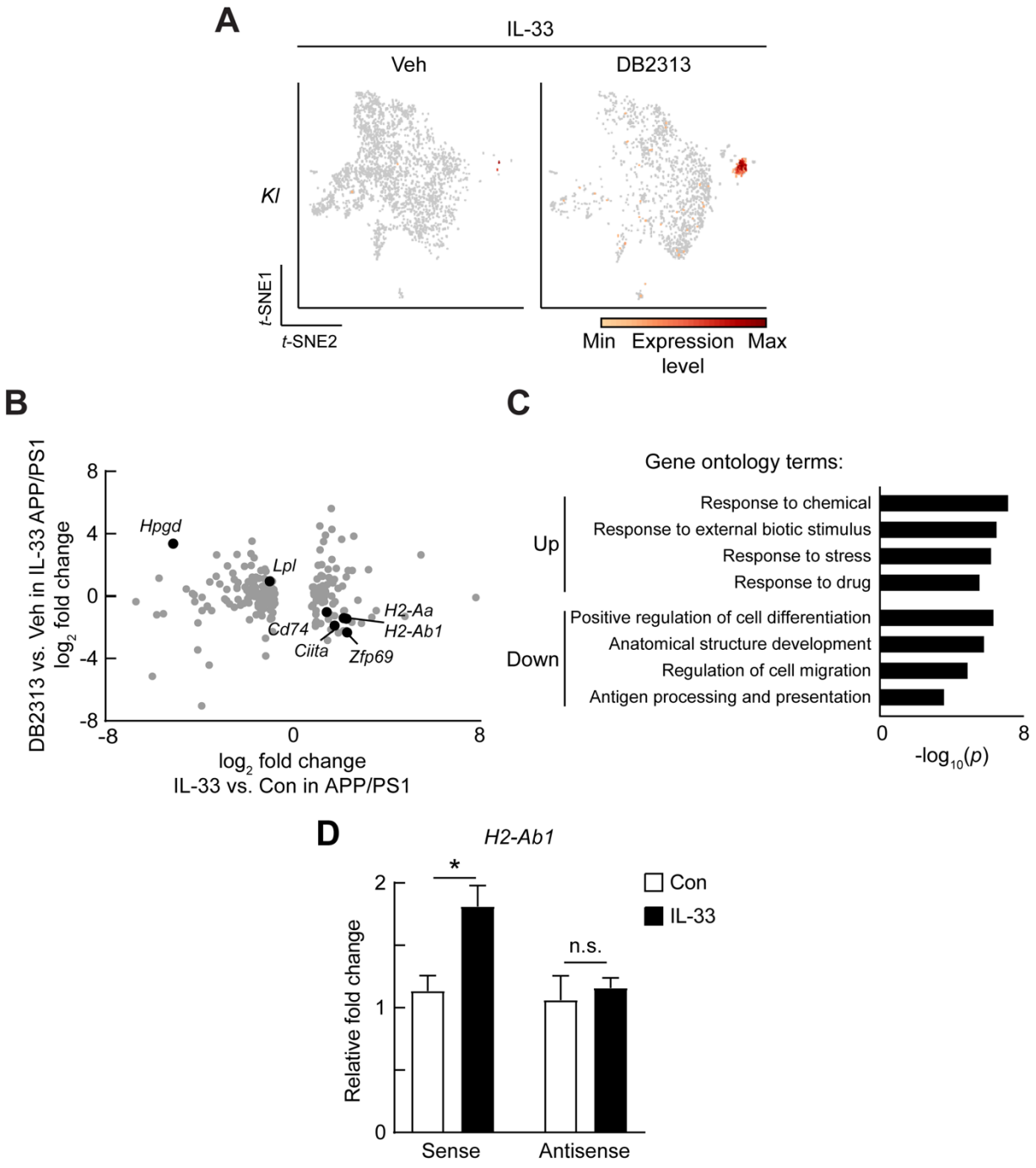

Figure S6. PU.1 inhibition reverts the IL-33–induced gene expression changes in microglia in APP/PS1 mice.

(A) t-SNE plots showing the expression of *Kl* in microglia of each condition. (B) Dotplot showing the expression changes of all IL-33 DEGs in IL-33–injected APP/PS1 mice upon DB2313 administration. (C) Pathway analysis of the DEGs in APP/PS1 mouse microglia after IL-33 injection with or without DB2313 administration. (D) Bar plot showing the expression change of *H2-Ab1*, a MHC-II gene, in BV2 cells after co-treatment of IL-33 and PU.1 antisense oligonucleotide.